JEM Journal of Experimental Medicine

ARTICLE

P2Y1 receptor blockade normalizes network dysfunction and cognition in an Alzheimer's disease model

Nicole Reichenbach[1], Andrea Delekate[1], Björn Breithausen[2], Kevin Keppler[1], Stefanie Poll[1], Theresa Schulte[1], Jan Peter[1], Monika Plescher[1], Jan N. Hansen[1], Nelli Blank[1], Armin Keller[1], Martin Fuhrmann[1], Christian Henneberger[1,2,3], Annett Halle[1,4], and Gabor C. Petzold[1,5]

Astrocytic hyperactivity is an important contributor to neuronal-glial network dysfunction in Alzheimer's disease (AD). We have previously shown that astrocyte hyperactivity is mediated by signaling through the P2Y1 purinoreceptor (P2Y1R) pathway. Using the APPPS1 mouse model of AD, we here find that chronic intracerebroventricular infusion of P2Y1R inhibitors normalizes astroglial and neuronal network dysfunction, as measured by in vivo two-photon microscopy, augments structural synaptic integrity, and preserves hippocampal long-term potentiation. These effects occur independently from β-amyloid metabolism or plaque burden but are associated with a higher morphological complexity of periplaque reactive astrocytes, as well as reduced dystrophic neurite burden and greater plaque compaction. Importantly, APPPS1 mice chronically treated with P2Y1R antagonists, as well as APPPS1 mice carrying an astrocyte-specific genetic deletion (Ip3r2$^{-/-}$) of signaling pathways downstream of P2Y1R activation, are protected from the decline of spatial learning and memory. In summary, our study establishes the restoration of network homoeostasis by P2Y1R inhibition as a novel treatment target in AD.

Introduction

Alzheimer's disease (AD) is a chronic and incurable neurodegenerative disease characterized by progressive β-amyloid (Aβ) and phosphorylated tau accumulation. Although the exact mechanisms underlying AD remain incompletely understood, neuronal dysfunction and degeneration appear to be sustained by a combination of detrimental factors that include vascular pathology, neuroinflammation, and the dysregulation of neuronal-glial networks (Heneka et al., 2015; Palop and Mucke, 2016). Aberrant network activity is an especially relevant target in AD, as it can be detected across the translational spectrum—from in vitro preparations to animal models and patients (Palop and Mucke, 2016)—and emerges at very early or even presymptomatic stages of the disease (Sperling et al., 2009). Hence, targeting network imbalance in AD holds the strong potential to delay clinical disease onset and slow symptom progression.

Most studies in animal models so far have focused on the disequilibrium of neuronal networks, which is characterized by seizures and a higher fraction of hyperactive neurons (Palop et al., 2007; Busche et al., 2008; Kuchibhotla et al., 2008). However, similar to neurons, astrocytes also become hyperactive in AD models. Astroglial hyperactivity is most prominent around Aβ plaques and, interestingly, occurs independently from neuronal activity (Kuchibhotla et al., 2009; Delekate et al., 2014). We have previously shown that nucleotides such as ATP and ADP, which are released in the proinflammatory environment around plaques, activate metabotropic P2Y1 purinoreceptors (P2Y1Rs) on astrocytes, leading to an increased frequency of spontaneous astroglial calcium events (Delekate et al., 2014). However, whether astrocytic hyperactivity ameliorates or aggravates the pathogenic pathways and cognitive sequelae of AD has remained unclear. Because astrocytes structurally and metabolically support normal synaptic function and contribute to the regulation of blood flow (Petzold and Murthy, 2011; Araque et al., 2014), the normalization of astroglial network imbalance may have profound consequences for neuronal function in AD. Therefore, we here aimed to investigate the effects of long-term P2Y1R inhibition in a mouse model of AD. We found that chronic treatment with P2Y1R antagonists normalized neuronal-astroglial network activity, restored structural and functional synaptic integrity, reduced neuritic dystrophy, and attenuated cognitive decline. These beneficial effects were associated with a higher morphological complexity of astrocytes around Aβ plaques and were in part recapitulated in mice lacking the IP3 receptor type 2 (IP3R2), i.e., the signaling downstream of P2Y1R activation,

[1]German Center for Neurodegenerative Diseases, Bonn, Germany; [2]Institute of Cellular Neurosciences, University Hospital Bonn, Bonn, Germany; [3]Institute of Neurology, University College London, London, England, UK; [4]Department of Neuropathology, University Hospital Bonn, Bonn, Germany; [5]Department of Neurology, University Hospital Bonn, Bonn, Germany.

Correspondence to Gabor C. Petzold: gabor.petzold@dzne.de.

© 2018 Reichenbach et al. This article is distributed under the terms of an Attribution–Noncommercial–Share Alike–No Mirror Sites license for the first six months after the publication date (see http://www.rupress.org/terms/). After six months it is available under a Creative Commons License (Attribution–Noncommercial–Share Alike 4.0 International license, as described at https://creativecommons.org/licenses/by-nc-sa/4.0/).

Downloaded from http://rupress.org/jem/article-pdf/215/6/1649/1760532/jem_20171487.pdf by guest on 08 February 2026

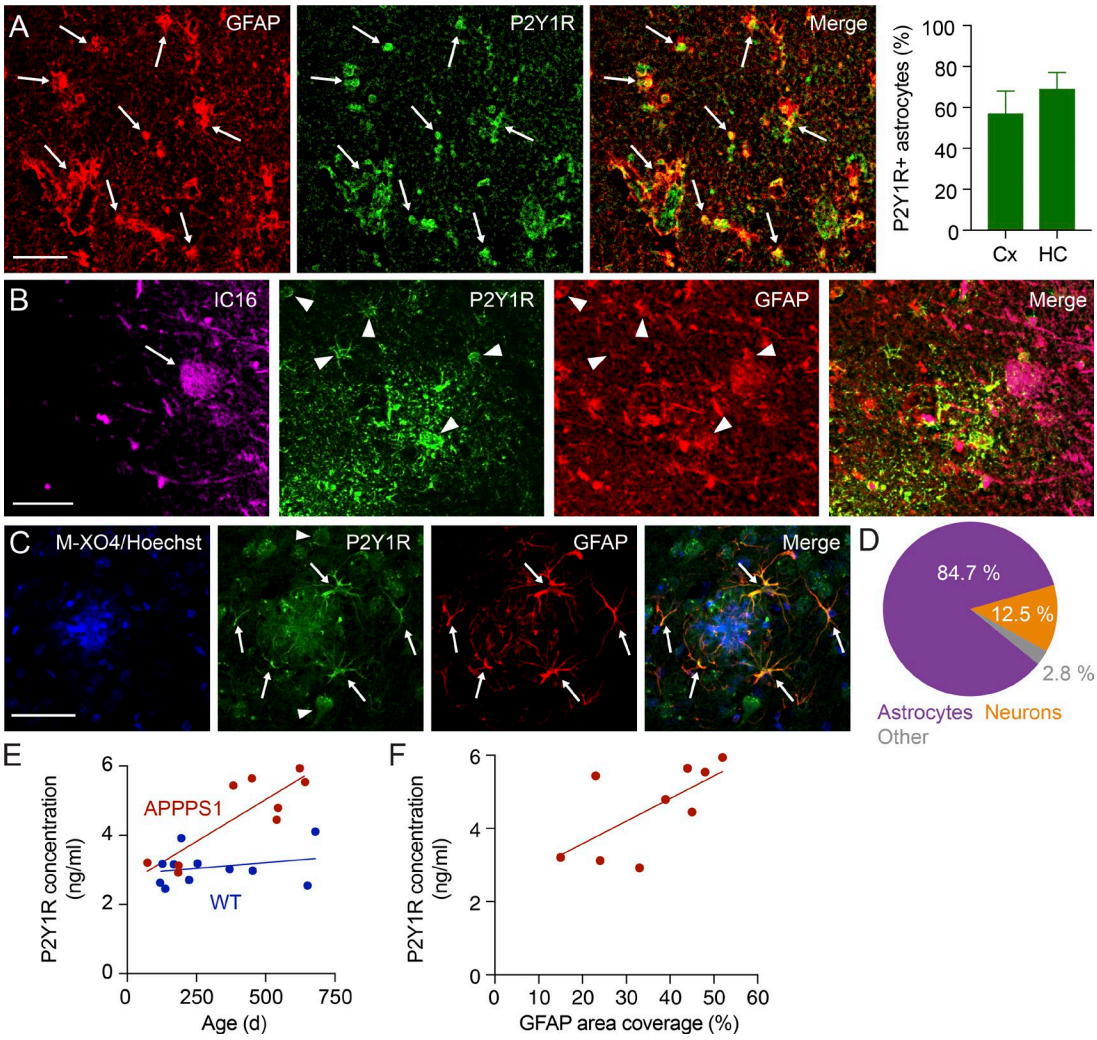

Figure 1. **P2Y1R expression in AD and APPPS1 mice. (A)** P2Y1R expression in cortical astrocytes (anti-GFAP; arrows) in human AD. Right: P2Y1R expression occurred in the majority of GFAP-positive astrocytes in cortex (CX) and hippocampus (HC; n = 211 cortical and 106 hippocampal astrocytes from four AD patient samples; mean ± SEM). **(B)** Reactive astrocytes (GFAP) around Aβ plaques (stained with IC16 antibody; arrow) in the cortex in human AD express P2Y1R (arrowheads). **(C)** In APPPS1 mice, P2Y1R are expressed by reactive astrocytes (arrows) around plaques (labeled with methoxy-X04) as well as neurons (arrowheads). Bars, 50 µm. **(D)** The majority of P2Y1R-positive cells were astrocytes, whereas neurons accounted for a smaller fraction (data are from n = 4 APPPS1 mice; age, 6 mo). **(E and F)** APPPS1 showed an age-dependent increase of P2Y1R concentration (Spearman correlation, ρ = 0.73) that correlated with progressive reactive astrogliosis (GFAP; ρ = 0.63). No increase was seen in WT littermates (ρ = 0.22; n = 9 APPPS1 vs. n = 11 WT mice).

altogether establishing astroglial P2Y1R as a potential treatment target in AD.

Results

P2Y1R is expressed by reactive astrocytes and neurons in human AD and APPPS1 mice

We used immunohistochemistry to determine the cell types expressing P2Y1R in human AD and APPPS1 mice. In postmortem cortical and hippocampal sections of neuropathologically confirmed cases of AD, we found that the majority of reactive astrocytes express P2Y1R (Fig. 1 A), including astroglia located around Aβ plaques (Fig. 1 B). A similar pattern was evident in APPPS1 mice, in which P2Y1R was predominantly expressed by reactive astrocytes around Aβ plaques (Fig. 1, C and D), as previously reported (Delekate et al., 2014). However, we also detected P2Y1R expression in neurons, although this contributed to a much smaller fraction of overall expression (Fig. 1, C and D). Moreover, in a P2Y1R-specific ELISA assay, the whole-brain concentration of P2Y1R strongly increased with age (Spearman correlation, ρ = 0.73) and with the level of astrocyte reactivity in APPPS1 mice (Spearman correlation, ρ = 0.63), but not in WT littermates (Fig. 1, E and F). We confirmed that astrocytes were not labeled by the antibody used in this study in brain sections from *P2ry1*$^{-/-}$ mice (Fig. S1).

Chronic P2Y1R inhibition reduces neuronal-astroglial network hyperactivity in APPPS1 mice

We have previously shown that acute P2Y1R inhibition reduces astroglial network hyperactivity in APPPS1 mice (Delekate et al., 2014). Therefore, we next explored whether chronic P2Y1R inhibition could persistently reduce cortical astroglial network activity in APPPS1 mice. To this end, we implanted osmotic minipumps to infuse the P2Y1R antagonist MRS2179 (Boyer et al., 1998) or vehicle

Downloaded from http://rupress.org/jem/article-pdf/215/6/1649/1760532/jem_20171487.pdf by guest on 08 February 2026

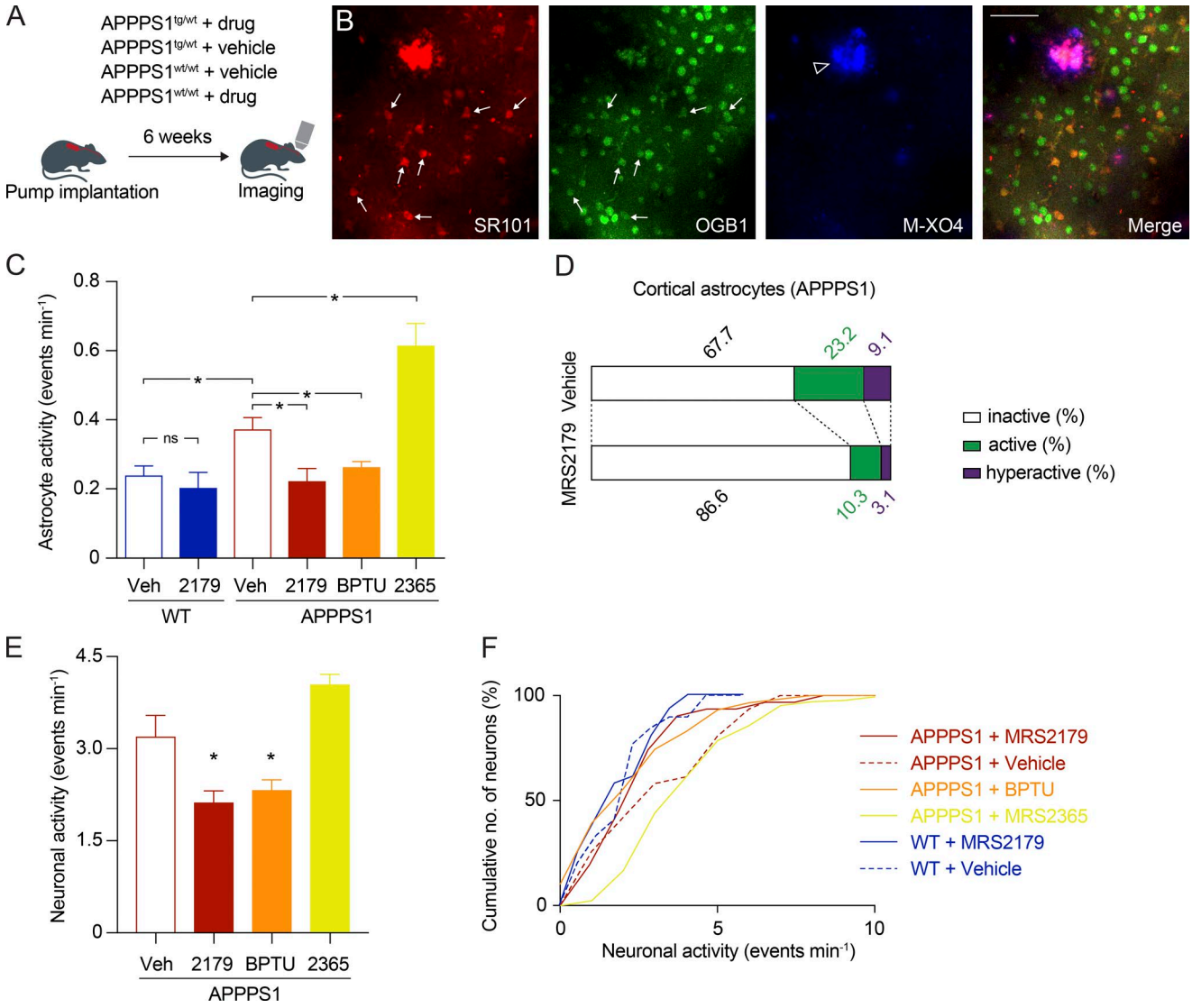

Figure 2. **Cortical astrocytes are hyperactive in APPPS1 mice, and MRS2179 reduces cortical hyperactivity. (A)** APPPS1 mice or WT littermates were treated with P2Y1R-selective drugs through osmotic minipumps for a total of 6 wk and imaged through cranial windows. **(B)** In vivo two-photon microscopy of calcium activity, measured with OGB-1, in astrocytes and neurons in the cortex of APPPS1 mice. Astrocytes were identified by SR101 colabeling (arrows). Aβ plaques were labeled with methoxy-X04 (arrowhead). Bar, 50 µm. **(C and D)** Astroglial hyperactivity was prominent in vehicle-treated (Veh) APPPS1 mice, but was reduced to levels similar to those of WT littermates in MRS2179-treated or BPTU-treated APPPS1 mice. In contrast, astroglial activity was significantly increased in MRS2365-treated mice (APPPS1 + MRS2179, *n* = 6 mice; APPPS1 + BPTU, *n* = 6 mice; APPPS1 + MRS2365, *n* = 6 mice; APPPS1 + vehicle, *n* = 6 mice; WT + MRS2179, *n* = 3 mice; WT + vehicle, *n* = 4 mice; age, 11 mo; *, P < 0.05, Kruskal–Wallis test followed by Dunn's multiple comparisons test; mean ± SEM). **(E and F)** The frequency of spontaneous neuronal events was significantly reduced by MRS2179 and BPTU and nonsignificantly increased by MRS2365 in transgenic mice (*, P < 0.05, Kruskal–Wallis test followed by Dunn's multiple comparisons test; same mice as in C; mean ± SEM). The cumulative distributions of spontaneous neuronal calcium transients in MRS2179-treated or BPTU-treated APPPS1 mice were not different from those of vehicle-treated or MRS2179-treated WT mice (P > 0.05, Kolmogorov–Smirnov test) but were significantly different from those of vehicle-treated or MRS2365-treated APPPS1 mice (P < 0.05, Kolmogorov–Smirnov test).

intracerebroventricularly (i.c.v.). After a 6-wk continuous treatment period, the mice were anesthetized and subjected to calcium imaging of cortical network activity using in vivo two-photon microscopy of the calcium indicator OGB-1 AM (Fig. 2, A and B). Astrocytes were identified by colabeling with sulforhodamine 101 (SR101), and plaques were labeled with methoxy-X04 (Fig. 2 B).

These experiments revealed that chronic P2Y1R inhibition in APPPS1 mice strongly reduced astroglial hyperactivity to levels similar to WT littermates (Fig. 2 C; Kruskal–Wallis test followed by Dunn's multiple comparisons test for all comparisons). MRS2179 had no significant effect on astrocyte activity in WT mice, indicating that P2Y1R inhibition does not nonspecifically dampen astroglial activity when pathological hyperactivity is absent. Moreover, chronic P2Y1R inhibition in APPPS1 mice resulted in a categorical shift in astroglial activity levels toward an inactive/normal-active phenotype (Fig. 2 D) typical for anesthetized WT animals (Thrane et al., 2012; Delekate et al., 2014). Hence, chronic P2Y1R inhibition normalizes cortical astrocytic network activity. In addition, as MRS2179 can also affect other purinoreceptors (Boyer et al., 1998), we also

Downloaded from http://rupress.org/jem/article-pdf/215/6/1649/1760532/jem_20171487.pdf by guest on 08 February 2026

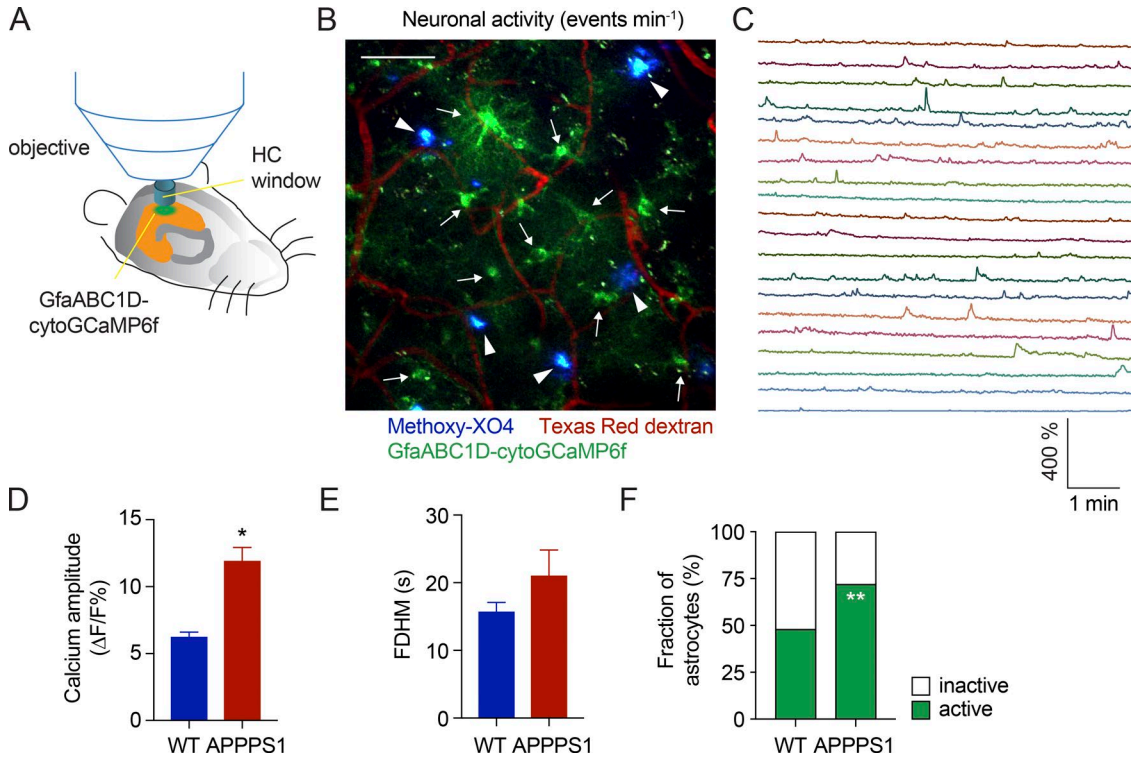

Figure 3. **Hippocampal astrocytes are hyperactive in APPPS1 mice. (A)** AAV-GfaABC1D-cytoGCaMP6f was injected into the dorsal hippocampus in APP PS1 mice or WT littermates, and a window above the right dorsal hippocampus (HC) was created for imaging. Mice were imaged 4 wk later. **(B)** Hippocampal astrocytes labeled with cytoGCaMP6f in vivo (arrows). Aβ plaques were labeled with methoxy-X04 (arrowheads). Blood vessels were labeled with Texas Red dextran. Bar, 50 µm. **(C)** Spontaneous calcium events in hippocampal astrocytes labeled with cytoGCaMP6f in vivo. Traces correspond to astrocytes displayed in Video 1. **(D–F)** Spontaneous calcium amplitudes of hippocampal astrocytes were higher in APPPS1 mice compared with WT littermates (*, P < 0.05, Mann–Whitney test; mean ± SEM), whereas the full duration at half maximum (FDHM) was similar. The fraction of active astrocytes was higher in APPPS1 mice (**, P < 0.001, Fisher's exact test; APPPS1, *n* = 149 cells from four mice, age, 11 mo; WT, *n* = 244 cells from six age-matched mice).

performed experiments using the P2Y1R antagonist BPTU, an allosteric inhibitor with a different binding site than MRS2179 and high selectivity over other P2Y and P2X receptors (Zhang et al., 2015). Mice treated for 6 wk with BPTU through osmotic minipumps also displayed reduced astroglial hyperactivity (Fig. 2 C). Moreover, we found that the P2Y1R agonist MRS2365 (Chhatriwala et al., 2004) increased network hyperactivity in chronically treated APPPS1 mice (Fig. 2 C).

Because neuronal network hyperexcitability is another hallmark of AD mouse models (Palop et al., 2007; Busche et al., 2008; Kuchibhotla et al., 2008), we also determined the effects of MRS2179, BPTU, and MRS2365 on cortical neuronal calcium activity. Interestingly, similar to astroglial activity, chronic treatment with MRS2179 and BPTU also led to a reduction of neuronal activity in plaque-bearing APPPS1 mice (P < 0.05, Kruskal–Wallis test followed by Dunn's multiple comparisons test and Kolmogorov–Smirnov test), whereas there was a trend toward higher neuronal activity in mice chronically treated with MRS2365 (Fig. 2, E and F).

Hippocampal astrocytes are hyperactive in APP PS1 mice in vivo

As astrocytic hyperactivity in previous studies (Kuchibhotla et al., 2009; Delekate et al., 2014) was investigated only in the cortex, but the behavioral phenotype of AD models largely correlates with hippocampal pathology, we aimed to establish whether and to what extent astrocytes in the hippocampus are also hyperactive. To this end, we injected adeno-associated virus (AAV) encoding the fluorescent calcium indicator GCaMP6f under the astrocytic GfaABC1D promoter into the hippocampus and imaged astroglial network activity 4 wk later using two-photon microscopy through a window that was surgically implanted above the right dorsal hippocampus (Fig. 3 A). Astrocytes were clearly identifiable by their GCaMP6f expression and were spontaneously active (Fig. 3, B and C; and Video 1) similar to cortical astrocytes. Compared with age-matched littermates, the amplitude of the calcium transients was significantly higher (P < 0.05, Mann–Whitney test) and the number of spontaneously active hippocampal astrocytes was increased in APPPS1 mice (P < 0.001, Fisher's exact test; Fig. 3, D–F). Because of the technically demanding surgical preparation of the hippocampal window, it was not possible to apply compounds topically or i.c.v. in these animals.

Chronic P2Y1R inhibition reverses synaptic deficits and restores structural synaptic integrity in the hippocampus

We next tested whether MRS2179 affects the well-established deficits of synaptic plasticity in the hippocampus of APPPS1 mice. Consistent with previous studies (Gengler et al., 2010), long-term potentiation (LTP) of CA3-CA1 Schaffer collateral

Downloaded from http://rupress.org/jem/article-pdf/215/6/1649/1760532/jem_20171487.pdf by guest on 08 February 2026

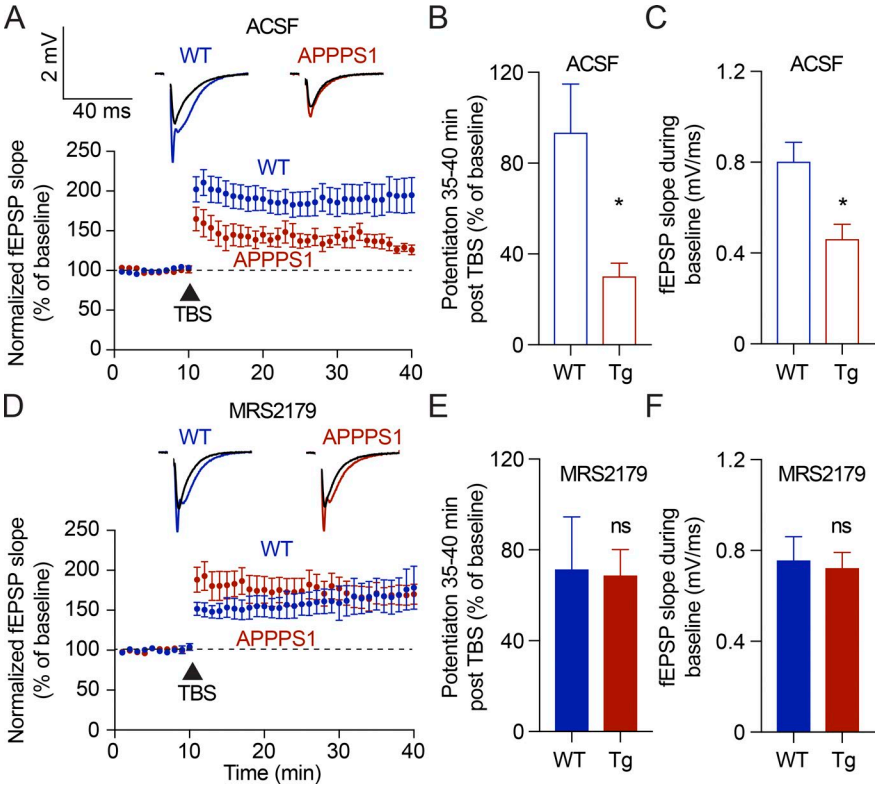

Figure 4. **MRS2179 restores hippocampal LTP in APPPS1 mice. (A)** Representative sample traces before and after LTP of CA3-CA1 Schaffer collateral synapses, and time courses of normalized fEPSP slopes during LTP, in slices perfused with ACSF from APPPS1 mice (red, *n* = 8 slices from three animals; age, 8 mo) compared with age-matched WT littermates (blue, *n* = 12 slices from three animals). **(B)** LTP, quantified as the fEPSP slope potentiation 35–40 min after TBS, was strongly reduced in APP PS1 (transgenic [Tg]) compared with WT mice (*, P < 0.05, Mann–Whitney test). **(C)** The strength of basal synaptic transmission, assessed by quantifying the baseline fEPSP slope, was reduced in APPPS1 compared with WT mice (*, P < 0.05, Mann–Whitney test). **(D–F)** LTP and basal synaptic transmission in slices from WT and APPPS1 animals were not significantly different in the presence of MRS2197 (30 µM; red, APPPS1, *n* = 8 slices from four animals; age, 8 mo; blue, age-matched WT, *n* = 11 slices from three animals; Mann–Whitney test for both comparisons). The effect of MRS2179 on WT slices was nonsignificant compared with ACSF-perfused slices (P = 0.31, Mann–Whitney test). All data are represented as mean ± SEM.

synapses was impaired in acute brain slices obtained from APPPS1 mice compared with slices from age-matched WT littermates (Fig. 4, A and B; P < 0.05, Mann–Whitney test). Moreover, basal synaptic transmission was also significantly impaired in slices from APPPS1 mice compared with slices from WT animals (Fig. 4 C; P < 0.05, Mann–Whitney test). Next, we tested in a second set of experiments whether this impairment is also observed in the presence of MRS2179. Importantly, the impairment of LTP, as well as the deficit in basal synaptic transmission, were not detected in the presence of MRS2179 (Fig. 4, D–F; P > 0.05, Mann–Whitney test for both comparisons).

To determine the effects of chronic MRS2179 treatment on hippocampal CA1 synapses, we performed high-resolution confocal microscopy analysis of the colabeled pre- and postsynaptic markers synaptophysin and Homer1—i.e., synaptic puncta (Shi et al., 2017)—in brain sections from APPPS1 mice and age-matched WT littermates (Fig. 5 A). As expected, there was a strong decrease in the density of synaptic puncta in vehicle-treated APPPS1 compared with WT mice, but interestingly, the density of synaptic puncta was restored to near-WT levels in APPPS1 mice chronically treated with MRS2179 (Fig. 5, A and B; Kruskal–Wallis test followed by Dunn's multiple comparisons test).

Moreover, to quantify dystrophic neurites around plaques, we used immunoreactivity for the lysosome component lysosomal associated membrane protein 1 (LAMP1) as an established proxy marker (Condello et al., 2011). We found that the area of dystrophic neurites was reduced in MRS2179-treated APPPS1 mice (Fig. 5, C and D; P < 0.05, Mann–Whitney test), indicating that normalization of aberrant network activity confers protection to periplaque neurites and synapses.

Chronic P2Y1R inhibition does not affect amyloid metabolism, but increases astroglial plaque barrier function

Because Aβ production can be influenced by network activity (Palop and Mucke, 2016) and P2Y1R activation may modulate glial reactivity (Franke et al., 2012), we next determined the effect of 6-wk MRS2179 treatment on Aβ metabolism and glial activation.

We found no effect on the overall area covered by GFAP-positive astrocytes or Iba1-positive microglia in the cortex or hippocampus of APPPS1 mice treated with MRS2179 compared with vehicle-treated mice (Fig. 6, A–D, I, and J; P > 0.05, Mann–Whitney test for all comparisons). Moreover, the treatment had no effect on cortical and hippocampal Aβ plaque load and size (Fig. 6, E–H and K–M; P > 0.05, Mann–Whitney test for all comparisons), as measured by IC16 antibody or thioflavin staining. Similarly, levels of soluble as well as insoluble $A\beta_{1-40}$ and $A\beta_{1-42}$, determined using an electrochemiluminescence immunoassay after sequential extraction with radioimmunoprecipitation assay (RIPA) and SDS buffer, were comparable between the two groups (Fig. 6, N and O; P > 0.05, Mann–Whitney test for all comparisons). The levels of full-length amyloid precursor protein (APP) and its C-terminal fragments (CTFs), as well as levels of the APP-degrading enzyme neprilysin/CD10, were similar in all groups (Fig. 6, P–T; P > 0.05, Mann–Whitney test for all comparisons).

Because glial cells form a dense anatomical barrier around Aβ plaques that may help contain the diffusion of neurotoxic Aβ fibrils (Condello et al., 2015; Yuan et al., 2016), we also determined morphological changes of astrocytes and microglia in the periplaque region. We found that the mean plaque intensity—an established marker of plaque compaction that is inversely correlated with toxic fibril surface area (Condello et al., 2015)—was increased in MRS2179-treated APPPS1 mice (Fig. 7 A; P < 0.05, Mann–Whitney

Downloaded from http://rupress.org/jem/article-pdf/215/6/1649/1760532/jem_20171487.pdf by guest on 08 February 2026

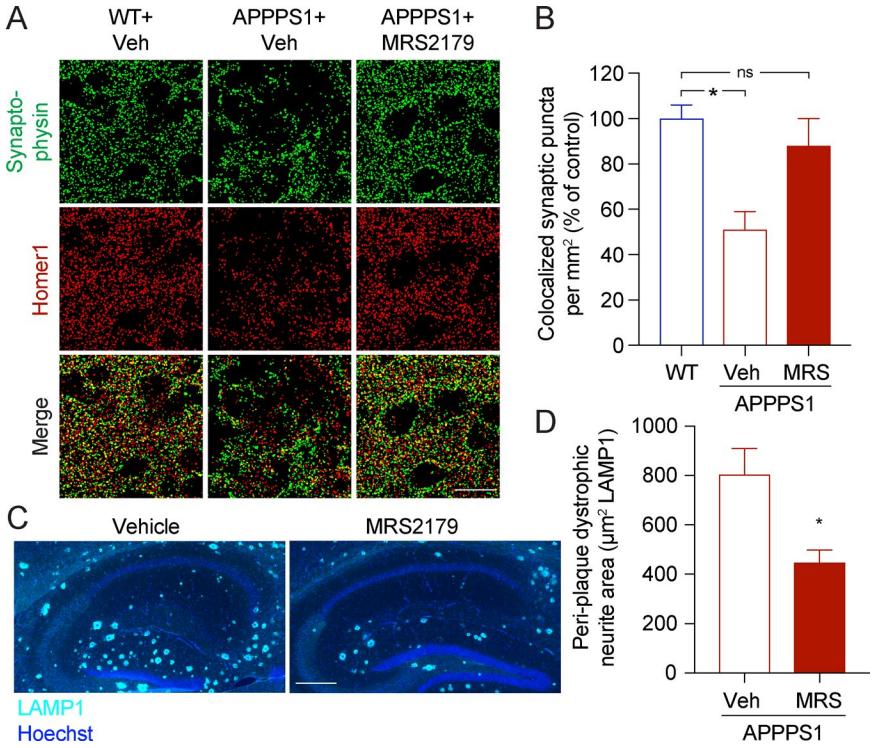

Figure 5. **MRS2179 augments structural synaptic integrity. (A and B)** The density of hippocampal CA1 synaptic puncta, quantified as colocalization of synaptophysin and Homer1 immunoreactivity, was reduced in vehicle-treated APPPS1 mice (Veh) compared with WT littermates, but similar to WT in MRS2719-treated APPPS1 mice (APPPS1 + MRS2719, *n* = 5 mice; APPPS1 + vehicle, *n* = 5 mice; WT, *n* = 4 mice; age of all groups, 11 mo; *, P < 0.05, Kruskal–Wallis test followed by Dunn's multiple comparisons test; mean ± SEM). Bar, 20 µm. **(C and D)** The periplaque area covered by dystrophic neurites, measured by LAMP1 immunoreactivity, was reduced in MRS2179-treated compared with vehicle-treated APPPS1 mice (APPPS1 + MRS2719, *n* = 5 mice; APPPS1 + vehicle, *n* = 4 mice; age of both groups, 11 mo; *, P < 0.05, Mann–Whitney test; mean ± SEM). Bar, 300 µm.

test), perhaps explaining the reduction in dystrophic neurite area. Moreover, chronic MRS2179 treatment significantly increased the density and length of astrocytic process branches and terminal process points in the periplaque region and led to an increase in the number of periplaque complex astroglial structures (Fig. 7, B–E, J, and K; P < 0.05, Mann–Whitney test for all comparisons; representative examples are given in Fig. S2). No major changes of these parameters were observed in periplaque microglia (Fig. 7, F–K; P > 0.05, Mann–Whitney test for all comparisons), indicating that the effects of P2Y1R inhibition are predominantly mediated by astrocytes.

Chronic P2Y1R inhibition improves learning and memory in APPPS1 mice

Next, we determined the effects of chronic pharmacological treatment on hippocampus-dependent spatial reference learning and memory. To ensure compatibility with the osmotic minipump implantation, we used the Barnes maze test paradigm, in which mice are trained to memorize the location of a hidden escape box (Pompl et al., 1999). We compared APPPS1 mice treated with MRS2179, BPTU, MRS2365, or vehicle with age-matched WT mice treated with MRS2179 or vehicle. Behavioral testing commenced 5 wk after pump implantation (Fig. 8 A). During the 4-d acquisition period, the temporal latency and spatial distance covered by the mice until they reached the escape box was similar in all groups except for APPPS1 treated with the P2Y1R agonist MRS2365, which displayed longer latencies and distances compared with WT mice (Fig. 8, B–E; P < 0.05, two-way repeated-measures ANOVA and Bonferroni post hoc test and Kruskal–Wallis test followed by Dunn's multiple comparisons test, respectively). Moreover, and perhaps more importantly, vehicle-treated as well as MRS2365-treated APPPS1 mice relied on a nonspatial (serial) search strategy, indicated by the continuously high number of serial errors performed before locating the escape box (Fig. 8, F–H; P < 0.05, two-way repeated-measures ANOVA and Bonferroni post hoc test and one-way ANOVA and Dunnett's multiple comparison test, respectively). In contrast, MRS2179-treated as well as BPTU-treated APPPS1 mice, similar to WT littermates, switched from a nonspatial to a (targeted) spatial search strategy within 1–2 d (Fig. 8, F–H), indicating that P2Y1R inhibition improved spatial learning in APPPS1 mice. 24 h after the last acquisition day, mice were subjected to a probe trial in which the escape box was removed. As expected, spatial memory was strongly impaired in APPPS1 mice treated with vehicle or MRS2365 (Fig. 8 I; Wilcoxon matched-pairs signed rank test and Kruskal–Wallis test followed by Dunn's multiple comparisons test, respectively). However, MRS2179-treated as well as BPTU-treated APPPS1 mice spent significantly more time in the target quadrant, comparable to WT mice, indicating that spatial memory was improved in these mice (Fig. 8 I). Motor function, measured by the velocity of mice across all days, was similar in all groups (Fig. 8 J; P > 0.05, Kruskal–Wallis test followed by Dunn's multiple comparisons test).

Astrocyte-specific deletion of metabotropic signaling attenuates network dysfunction and improves spatial memory

Finally, to establish whether these effects were mediated by astrocytic P2Y1R, as opposed to nonastroglial sources of P2Y1R or ionotropic purinoreceptors, we used mice lacking IP3R2 (*Ip3r2*$^{-/-}$; Li et al., 2005). IP3R2 is the predominant IP3 receptor subtype in astrocytes but shows negligible expression in neurons (Sharp et al., 1999), thus representing a valid genetic model to study the contribution of signaling pathways downstream of astroglial metabotropic receptors such as P2Y1R. Spatial learning and memory

Downloaded from http://rupress.org/jem/article-pdf/215/6/1649/1760532/jem_20171487.pdf by guest on 08 February 2026

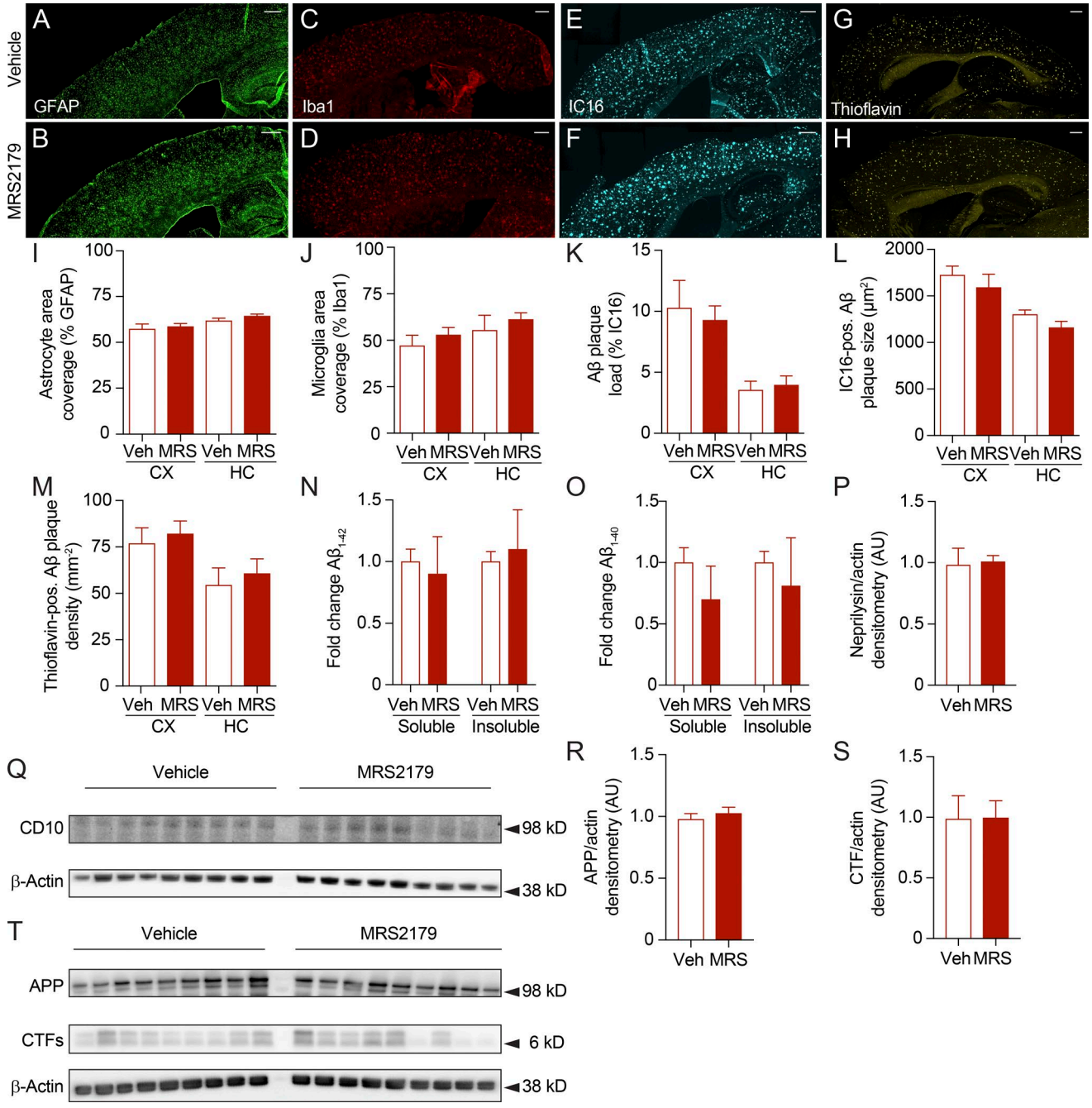

Figure 6. **Chronic P2Y1R inhibition has no effects on gliosis, plaque load, and amyloid metabolism. (A–M)** MRS2179 (in comparison to vehicle; *n* = 6 mice for each group; age of both groups, 9 mo) had no effect on reactive astrogliosis (anti-GFAP) or microgliosis (anti-Iba1). Similarly, no effects were seen on Aβ plaque load and size (IC16 staining) or the density of thioflavin-positive Aβ plaques (P > 0.05, Mann–Whitney test for all comparisons). Cortex (CX) and hippocampus (HC) were investigated separately. Bars, 200 µm. Veh, vehicle-treated. **(N and O)** Electrochemiluminescence ELISA after sequential extraction from whole-brain homogenates using RIPA and SDS buffer revealed no difference in soluble and insoluble $A\beta_{1-42}$ and $A\beta_{1-40}$ between APPPS1 mice treated with MRS2179 or vehicle (*n* = 6 mice for each group; P > 0.05, Mann–Whitney test for all comparisons). **(P–T)** Densitometric quantification of the Aβ-degrading enzyme neprilysin/CD10, APP, and CTFs normalized to β-actin showed similar expression in MRS2179-treated and vehicle-treated APPPS1 mice (*n* = 6 mice for each group; P > 0.05, Mann–Whitney test for all comparisons). All data are represented as mean ± SEM.

testing, as assessed using the Morris water maze paradigm, showed that the latency to find the hidden platform was significantly shorter in *Apppsl*$^{+/-}$ × *Ip3r2*$^{-/-}$ compared with *Apppsl*$^{+/-}$ × *Ip3r2*$^{+/+}$ mice, but similar to *Apppsl*$^{-/-}$ × *Ip3r2*$^{-/-}$ littermates (Fig. 9, A and B; two-way repeated-measures ANOVA and Bonferroni post hoc test and one-way ANOVA followed by Holm–Sidak's multiple comparisons test, respectively). In the probe trial, assessed 24 h after the last acquisition day, *Apppsl*$^{+/-}$ × *Ip3r2*$^{-/-}$ and *Apppsl*$^{-/-}$ × *Ip3r2*$^{-/-}$ mice spent more time in the target quadrant compared with nontarget quadrants, whereas *Apppsl*$^{+/-}$ × *Ip3r2*$^{+/+}$ mice spent equal times in target and nontarget quadrants (Fig. 9 C; Kruskal–Wallis test followed by Dunn's multiple comparisons test), indicating that

Downloaded from http://rupress.org/jem/article-pdf/215/6/1649/1760532/jem_20171487.pdf by guest on 08 February 2026

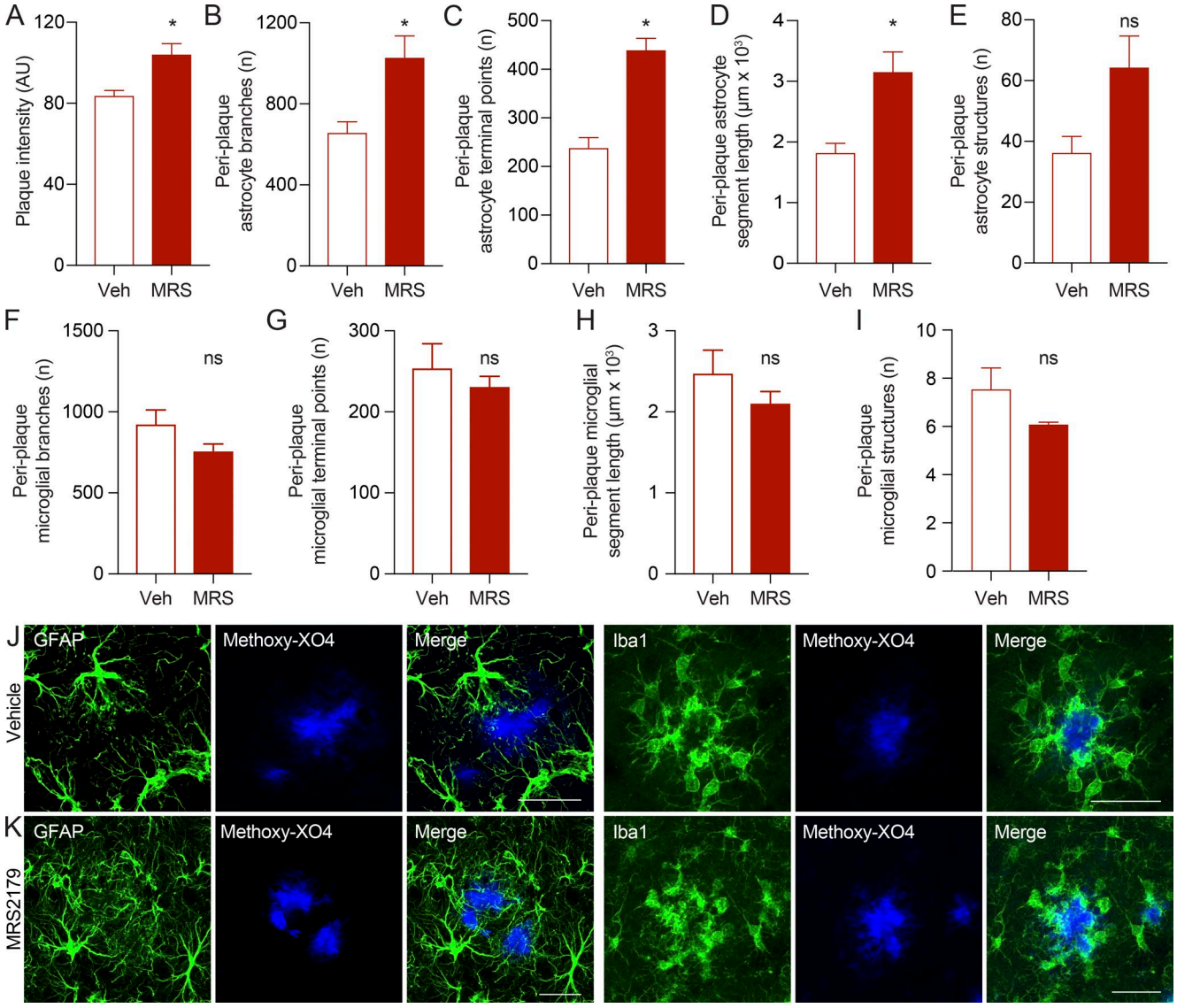

Figure 7. **P2Y1R inhibition increases the morphological barrier function of periplaque hippocampal astrocytes. (A)** The mean intensity of hippocampal plaques was increased in MRS2179-treated versus vehicle-treated (Veh) APPPS1 mice, indicating greater compaction of plaques induced by the drug (n = 5 mice for each group; age of both groups, 11 mo; *, $P < 0.05$, Mann–Whitney test). **(B–E)** The number and terminal points of near-plaque astrocyte branches and the length of astrocyte segments were increased by the drug treatment, and there was a trend toward more complex astrocytic structures around plaques (*, $P < 0.05$, Mann–Whitney test for all comparisons; mean ± SEM). **(F–I)** No significant changes in these parameters were seen in periplaque microglia ($P > 0.05$, Mann–Whitney test for all comparisons). **(J and K)** Representative examples. Astrocytes were labeled with anti-GFAP antibodies, microglia were labeled with anti-Iba1 antibodies, and plaques were labeled with methoxy-X04. Bars, 30 µm.

astroglial network normalization contributes to spatial memory restoration. Motor function, measured by the swimming velocity of mice across all days, was similar in all groups (Fig. 9 D; $P > 0.05$, Kruskal–Wallis test followed by Dunn's multiple comparisons test).

To confirm that astroglial hyperactivity was attenuated, we subjected these mouse lines to calcium imaging of cortical network activity using two-photon microscopy and found that, as expected, astroglial activity was strongly reduced in *Apppsl*$^{+/-}$ × *Ip3r2*$^{-/-}$ compared with *Apppsl*$^{+/-}$ × *Ip3r2*$^{+/+}$ mice, but similar to *Apppsl*$^{-/-}$ × *Ip3r2*$^{-/-}$ mice (Fig. 9 E; Kruskal–Wallis test followed by Dunn's multiple comparisons test). Moreover, topical application of the P2Y1R agonist MRS2365 had no significant effect on network activity in *Apppsl*$^{+/-}$ × *Ip3r2*$^{-/-}$ mice (Fig. 9 E), confirming sufficient functional suppression of the P2Y1R pathway in these mice.

Discussion

Aberrant network activity is an early and perhaps causal factor in cognitive decline and pathological synaptic remodeling, both of which are classical hallmarks of AD. Importantly, network disequilibrium is evident not only in animal models of AD (Busche et al., 2008; Kuchibhotla et al., 2008; Sanchez et al., 2012), but also in presymptomatic and symptomatic patients with AD (Sperling et al., 2009; Reiman et al., 2012; Vossel et al., 2016). Interestingly, a large body of evidence suggests that network dysfunction is a pathogenic component of AD, and not simply an intrinsic compensation for synaptic decline (Palop and Mucke, 2016).

Similar to neurons, astrocytes form organized large-scale networks (Araque et al., 2014). In AD, astrocytes adopt a reactive

Downloaded from http://rupress.org/jem/article-pdf/215/6/1649/1760532/jem_20171487.pdf by guest on 08 February 2026

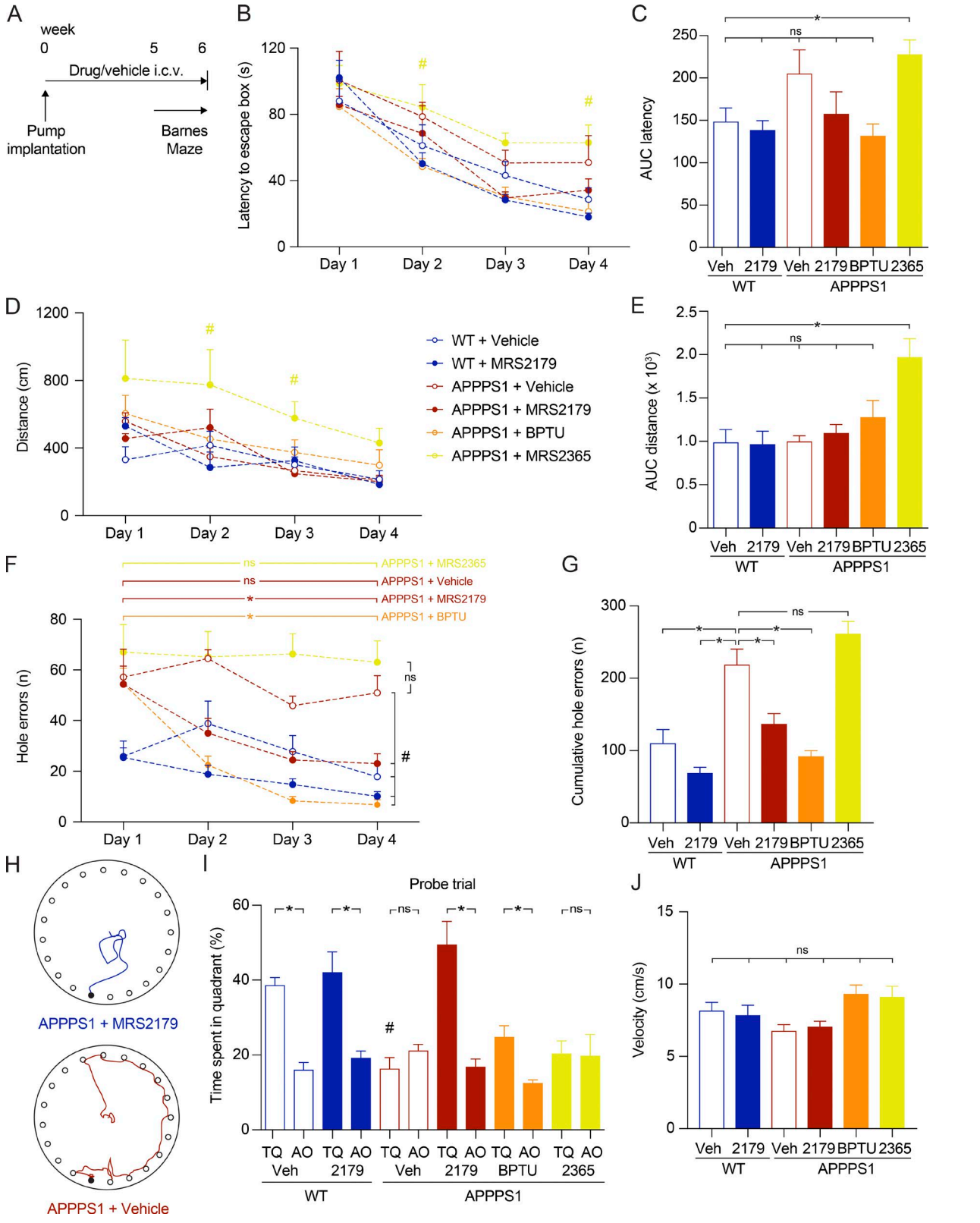

Figure 8. **Chronic P2Y1R inhibition reverses spatial reference learning and memory deficits in APPPS1 mice. (A)** Mice were treated with P2Y1R-selective drugs or vehicle through osmotic minipumps for 5 wk and tested in the Barnes maze test during continuous pump infusion. **(B)** The learning curve of the latency to the escape box was similar in all groups except for MRS2365-treated APPPS1 mice, which showed longer latencies compared with WT mice on days 2 and 4 (#, $P < 0.05$, two-way repeated-measures ANOVA and Bonferroni post hoc test). Data points represent the mean performance of mice during four trials/d (APPPS1 + MRS2179, $n = 8$ mice; APPPS1 + vehicle, $n = 8$ mice; APPPS1 + BPTU, 11 mice; APPPS1 + MRS2365, 7 mice; WT + MRS2179, $n = 8$ mice; WT + vehicle, $n = 7$ mice; age of all groups, 10–12 mo). **(C)** The area under the curve (AUC) for the latency to the escape box was higher in MRS2365-treated APPPS1 mice and similar in all other groups (*, $P < 0.05$, Kruskal–Wallis test followed by Dunn's multiple comparisons test). Veh, vehicle-treated. **(D and E)** The learning curve of the moved distance

Downloaded from http://rupress.org/jem/article-pdf/215/6/1649/1760532/jem_20171487.pdf by guest on 08 February 2026

phenotype, suggesting that this morphological alteration may also be accompanied by functional changes. Indeed, although spontaneous calcium events in astrocytes are rare in anesthetized WT animals (Thrane et al., 2012), the astroglial network becomes hyperactive in animal models of AD, especially in the vicinity of Aβ plaques (Kuchibhotla et al., 2009; Delekate et al., 2014), indicating that, similar to neurons, astrocytic network dysfunction may also contribute to AD pathogenesis. We have previously shown that astrocyte overactivation through P2Y1R accounts for a large part of astroglial hyperactivity (Delekate et al., 2014). In the present study, we found that reactive astrocytes account for the majority of P2Y1R expression in APPPS1 mice, and that long-term treatment with a P2Y1R inhibitor normalizes astroglial network activity to levels normally detected in WT animals. Importantly, this astrocytic network normalization also reduced neuronal hyperactivity. Although this effect could be related to P2Y1R expression by a subpopulation of neurons, reactive astrogliosis itself may also induce neuronal hyperexcitability (Ortinski et al., 2010; Robel and Sontheimer, 2016), suggesting that the attenuation of astrocytic network activity by P2Y1R inhibition may also modulate neuronal networks. In this regard, it is interesting to note that astrocytic P2Y1R have been shown to stimulate astroglial glutamate release and shape synaptic transmission (Domercq et al., 2006; Jourdain et al., 2007). In addition, although microglia remained largely unaffected morphologically by P2Y1R inhibition, some of the observed effects may still be mediated by microglia through astrocyte-to-microglia signaling (Liddelow et al., 2017). Although these mechanisms will have to be addressed by future studies, the net effect of this astroglial-neuronal network normalization by long-term P2Y1R inhibition is that synaptic integrity and function are preserved. Remarkably, this structural protection is paralleled by a restoration of hippocampal LTP, i.e., a cellular correlate of learning and memory. Moreover, we showed that this treatment restored spatial learning and memory. This effect appeared to be related to an improvement in hippocampal function, as APPPS1 mice treated with two pharmacologically different antagonists were able to use spatial search strategies, whereas vehicle-treated or agonist-treated transgenic mice were not. Although future studies using cell-specific deletion of P2Y1R will be necessary to dissect the individual contribution of astroglia and neurons, our data that APPPS1 mice carrying an astrocyte-selective deletion of the metabotropic signaling pathways downstream of P2Y1R show a similar protection from cognitive decline strongly suggest a primary role for astrocytes.

These effects occurred in mice at a late stage of Aβ deposition in that model and were not paralleled by detectable changes in plaque size or load, or in the levels of soluble or insoluble Aβ. Interestingly, however, the treatment led to an increase of the cellular complexity of reactive astrocytes in the direct vicinity of plaques, although the glial marker used in this study represents only a fraction of the total astrocytic process length, and ultrastructural studies are needed to fully explore this question. Moreover, the higher astroglial complexity was paralleled by greater plaque compaction, indicating that modulation of the astrocytic barrier function can help contain the toxic effects of Aβ species on periplaque neurites.

Taken together, our study underlines the potential of harnessing the astrocytic "arsenal" as a powerful tool to alleviate and perhaps prevent the pathological and cognitive sequelae of AD. Together with previous studies (Sanchez et al., 2012), our data also strengthen the hypothesis that aberrant network activity itself is an important contributor to pathological synaptic remodeling and cognitive decline in AD. Hence, purinoreceptor inhibitors may represent attractive candidates to investigate the effects of astroglial-neuronal network normalization on AD in further preclinical and clinical trials.

Materials and methods

Animals

All experiments were performed according to animal care guidelines and approved by the Landesamt für Natur, Umwelt und Verbraucherschutz of North Rhine-Westphalia (Germany). We used mice that coexpress the human KM67/671NL mutation in the APP (APPswe) and human L166P-mutated PS1 under the control of the Thy1 promoter on a C57BL/6J background (APPPS1-21; provided by M. Jucker, DZNE, Tübingen, Germany; Radde et al., 2006) and their WT age-matched and sex-matched littermates, as well as *Ip3r2*$^{-/-}$ (Li et al., 2005; provided by J. Chen, University of San Diego, San Diego, CA). *Ip3r2*$^{-/-}$ mice were crossed with *Apppsl*$^{+/-}$ mice, and *Apppsl*$^{+/-}$ × *Ip3r2*$^{+/-}$ and *Apppsl*$^{-/-}$ × *Ip3r2*$^{+/-}$ offspring were crossed to generate *Apppsl*$^{+/-}$ × *Ip3r2*$^{-/-}$, *Apppsl*$^{-/-}$ × *Ip3r2*$^{-/-}$, and *Apppsl*$^{+/-}$ × *Ip3r2*$^{+/+}$ for experiments. Animals were housed in groups on a 12-h light/dark cycle with food and water available ad libitum. Fixed brains of *P2y1r*$^{-/-}$ mice were provided

was similar in all groups except for MRS2365-treated APPPS1 mice, which moved longer distances to reach the escape box compared with WT mice on days 2 and 3 (#, P < 0.05, two-way repeated-measures ANOVA and Bonferroni post hoc test). Similarly, the AUC for the distance moved to the escape box was higher in MRS2365-treated APPPS1 mice and similar in all other groups (*, P < 0.05, Kruskal–Wallis test followed by Dunn's multiple comparisons test). **(F)** The number of "hole errors" as a measure of nonspatial over spatial search strategies was higher on day 4 in vehicle-treated APPPS1 and MRS2365-treated mice compared with MRS2179-treated or BPTU-treated APPPS1 mice as well as MRS2179-treated or vehicle-treated WT mice (#, P < 0.05, two-way repeated-measures ANOVA and Bonferroni post hoc test). Moreover, MRS2179-treated and BPTU-treated APPPS1 mice as well as both WT groups made significantly fewer errors on day 4 versus day 1 (P < 0.001), whereas vehicle-treated APPPS1 mice did not (*, P < 0.05, two-way repeated-measures ANOVA and Bonferroni post hoc test). **(G)** Cumulative hole errors across all days were higher in vehicle-treated APPPS1 mice compared with all other groups, but similar to MRS2365-treated APPPS1 mice (*, P < 0.05, one-way ANOVA and Dunnett's multiple comparison test). **(H)** Targeted (spatial) versus serial (nonspatial) search strategies in MRS2179-treated and vehicle-treated transgenic mice. **(I)** Probe trial data. The percentage of time mice spent in the target quadrant (TQ) was different from chance (P < 0.05, one-tailed one-sample *t* test) except in vehicle-treated and MRS2365-treated APPPS1 mice. Vehicle-treated and MRS2365-treated APPPS1 mice did not show a preference for the TQ compared with all other quadrants (AO; *, P < 0.05, Wilcoxon matched-pairs signed rank test), and time spent in the TQ was significantly less for vehicle-treated APPPS1 mice compared with WT mice (#, P < 0.05, Kruskal–Wallis test followed by Dunn's multiple comparisons test). **(J)** Velocity of mice in the Barnes maze across all days was similar in all groups (P > 0.05, Kruskal–Wallis test followed by Dunn's multiple comparisons test). All data are represented as mean ± SEM.

Downloaded from http://rupress.org/jem/article-pdf/215/6/1649/1760532/jem_20171487.pdf by guest on 08 February 2026

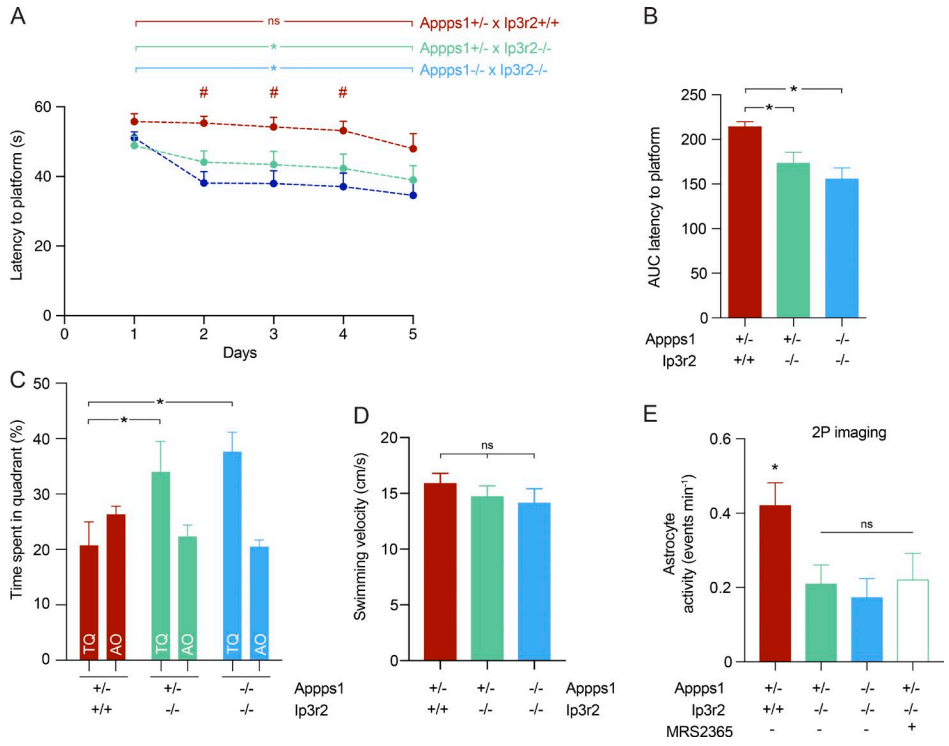

Figure 9. **Deletion of metabotropic signaling downstream of astrocyte P2Y1R activation improves spatial memory and network hyperactivity. (A)** *Appps1*$^{+/-}$ × *Ip3r2*$^{-/-}$ mice showed faster latencies to reach the hidden platform compared with *Appps1*$^{+/-}$ × *Ip3r2*$^{+/+}$ mice (#, P < 0.05, two-way repeated-measures ANOVA and Bonferroni post hoc test). Moreover, they showed a similar learning curve as *Appps1*$^{-/-}$ × *Ip3r2*$^{-/-}$ mice, indicated by significantly shorter latencies on the last acquisition day compared with the first acquisition day, whereas no significant differences between these days were seen in *Appps1*$^{+/-}$ × *Ip3r2*$^{+/+}$ mice (*, P < 0.05, two-way repeated-measures ANOVA and Bonferroni post hoc test; *Appps1*$^{+/-}$ × *Ip3r2*$^{-/-}$, *n* = 19 mice; *Appps1*$^{+/-}$ × *Ip3r2*$^{+/+}$, *n* = 10 mice; *Appps1*$^{-/-}$ × *Ip3r2*$^{-/-}$, *n* = 21 mice; age of all groups, 8–9 mo). Data points represent the mean performance of mice during four trials/d. **(B)** The area under the curve (AUC) for the latency to reach the hidden platform was similar in *Appps1*$^{+/-}$ × *Ip3r2*$^{-/-}$ and *Appps1*$^{-/-}$ × *Ip3r2*$^{-/-}$, but higher in *Appps1*$^{+/-}$ × *Ip3r2*$^{+/+}$, mice (*, P < 0.05, one-way ANOVA followed by Holm–Sidak's multiple comparisons test). **(C)** In the probe trial, the percentage of time mice spent in the target quadrant (TQ) was different from chance in *Appps1*$^{+/-}$ × *Ip3r2*$^{-/-}$ and *Appps1*$^{-/-}$ × *Ip3r2*$^{-/-}$ mice (P < 0.05, one-tailed one-sample *t* test), but not in *Appps1*$^{+/-}$ × *Ip3r2*$^{+/+}$ mice. Moreover, *Appps1*$^{+/-}$ × *Ip3r2*$^{+/+}$ spent significantly less time in the TQ compared with *Appps1*$^{+/-}$ × *Ip3r2*$^{-/-}$ and *Appps1*$^{-/-}$ × *Ip3r2*$^{-/-}$ mice (*, P < 0.05, Kruskal–Wallis test followed by Dunn's multiple comparisons test). **(D)** Swimming velocity of mice in across all days was similar in all groups (P > 0.05, Kruskal–Wallis test followed by Dunn's multiple comparisons test). **(E)** Activity of cortical astrocytes, measured using in vivo two-photon (2P) microscopy, in *Appps1*$^{+/-}$ × *Ip3r2*$^{-/-}$ mice was similar to *Appps1*$^{-/-}$ × *Ip3r2*$^{-/-}$ mice and significantly lower than in *Appps1*$^{+/-}$ × *Ip3r2*$^{+/+}$ mice. Application of the P2Y1R agonist MRS2365 did not change astroglial activity in *Appps1*$^{+/-}$ × *Ip3r2*$^{-/-}$ mice, indicating effective suppression of signaling downstream of astrocytic P2Y1R activation (*, P < 0.05, Kruskal–Wallis test followed by Dunn's multiple comparisons test). All data are represented as mean ± SEM.

by S. Koizumi (University of Yamanashi, Yamanashi, Japan) and U. Krügel (University of Leipzig, Leipzig, Germany).

Intracerebroventricular cannulation and drug treatment

MRS2179 (1 mM; Tocris) and MRS2365 (50 µM; Tocris) were solubilized in sterile saline; BPTU (10 µM; Tocris) was solubilized in DMSO and sterile saline. Mice were implanted s.c. at the interscapular region with osmotic minipumps (model Alzet 2006; delivery rate, 0.15 µl/h for 42 d; Durect) connected to Alzet Brain Infusion Kit 3 (anteroposterior [AP] −0.2 mm, medial lateral [ML] +1 mm relative to bregma; dorsal ventral [DV] +2.5 mm from the brain surface; Durect) for i.c.v. delivery. During surgery, animals were anesthetized with a combination of isoflurane (1.5% vol/vol), O_2 (0.3% vol/vol), and N_2O (0.7% vol/vol) and kept on a heating pad (37°C). Buprenorphine s.c. was used as an analgesic. Pumps were filled with saline or compounds according to the manufacturer's instructions.

For topical drug treatment, the dura was removed, and MRS2365 (0.5 µM; solubilized in sterile saline) was topically applied for 45 min. Agarose (1.5% in artificial cerebrospinal fluid [ACSF], in mM: 132 NaCl, 3 KCl, 0.6 $MgCl_2$, 1.5 $CaCl_2$, 24.6 $NaHCO_3$, 3.7 glucose, 6.7 urea) was placed on top of the cortex for stabilization, and the window was closed with a cover glass (diameter, 5 mm) and sealed with silicone elastomer (Kwik-Sil; World Precision Instruments [WPI]).

Stereotactic virus injections

Mice were anesthetized with isoflurane (induction, 3%; maintenance, 1–1.5% vol/vol). Body temperature was maintained with a heating pad (37°C). Mice were placed in a stereotaxic frame, and a small hole (~0.3 mm) was drilled into the skull using a dental drill (coordinates: AP −1.9 mm and ML +1.25 mm relative to bregma). AAV5-GfaABC1D-cytoGCaMP6f.SV40 (1 µl; UPenn Vector Core) was injected at 0.1 µl/min into the dorsal hippocampus (DV +1 mm from brain surface) using a syringe with a 34G cannula (WPI) connected to a pump (Ultra Micro Pump; WPI). Mice received buprenorphine for analgesia (0.05 mg/kg for 3 d) and dexamethasone to prevent inflammation (0.2 mg/kg, once).

Downloaded from http://rupress.org/jem/article-pdf/215/6/1649/1760532/jem_20171487.pdf by guest on 08 February 2026

Hippocampal window preparation

Hippocampal window surgery was performed 2 wk after virus injection and 4 wk before imaging as described previously (Schmid et al., 2016). Animals were anesthetized with isoflurane (induction, 3%; maintenance, 1–1.5% vol/vol), and body temperature was maintained with a heating pad (37°C). Mice received s.c. analgesic (buprenorphine, 0.1 mg/kg), an anti-inflammatory drug (dexamethasone, 0.2 mg/kg), and an antibiotic (cefotaxime, 2 g/kg). After fixation in a stereotaxic frame, the skin was removed under sterile conditions, and a craniotomy (diameter, 3 mm) above the right somatosensory cortex (coordinates: AP −1.9 and ML +1.25 relative to bregma) was created with a dental drill. The dura was removed, and the somatosensory cortex was aspirated with a 21G needle attached to a 20-ml syringe with a flexible tube. When the external capsule of the hippocampus was reached, the alveus was carefully exposed using a 27G needle. The surface of the dorsal hippocampus was rinsed with sterile saline until bleeding stopped. Subsequently, a metal tube (diameter, 3 mm; height, 1.5 mm) sealed with a glass coverslip (diameter, 3 mm) was inserted, and the upper tube edge was glued to the skull bone using dental cement. The remaining exposed surface of the skull bone was sealed with dental cement, and a custom-made metal bar (z-stripe) was glued next to the metal tube. The z-stripe allowed repetitive repositioning in a custom-made head-holder for in vivo imaging under the two-photon microscope. After surgery, mice received an analgesic (buprenorphine, 0.1 mg/kg) for 3 d.

Cortical window preparation

Windows were implanted as described previously (Delekate et al., 2014). Briefly, animals were anesthetized with isoflurane (induction, 3%; maintenance, 1–1.5% vol/vol) and kept on a heating pad (37°C). After fixation in a stereotactic frame, the scalp was removed, and a craniotomy (diameter, 5 mm) was created above the left somatosensory cortex using a dental drill. Agarose (1.5% in ACSF) was placed on top of the cortex for stabilization, and the window was closed with a cover glass (diameter, 5 mm) and sealed with dental cement.

In vivo two-photon microscopy

Mice implanted with a hippocampal window were imaged using an upright two-photon microscope (LaVision Trim ScopeII) with a 16× objective (NA 0.8, Nikon LWD16x) and three nondescanned detectors with bandpass filters (617/73, 460/80, and 525/50 nm). Texas Red dextran (70 kD; 6.25 mg/ml; Invitrogen) was injected i.v. to visualize blood vessels. To visualize Aβ plaques, methoxy-X04 (2–5 mg/kg; Tocris; solubilized in PBS with 4% Cremophor EL) was injected i.p. 24 h before imaging. During imaging, mice were anesthetized with isoflurane and kept on a heating pad (37°C). Fluorophores were excited at 800 or 920 nm using a Titan Sapphire (Ti:Sa) laser (Chameleon Ultra II; Coherent; 140-fs pulse width, 80-MHz repetition). Z stacks were taken (250 × 250 × 300 µm; 816 px; z increment, 3 µm; pixel dwell time, 0.95 µs), and XY time-lapse series of astroglial calcium activity (260 × 260 µm; 259 px; pixel dwell time, 1.88 µs) were subsequently recorded for 10 min at 3.57 Hz at a depth of 100–200 µm beneath the hippocampal surface.

In mice implanted with a cortical window, the calcium-sensitive dye OGB-1 AM (Life Technologies; solubilized in 20% Pluronic/80% DMSO and diluted to 1 mM with PBS) and SR101 (100 µM; Sigma) were coinjected into the cortex at a depth of 100–200 µm using glass micropipettes (tip diameter, 4–10 µm; WPI) connected to a pneumatic injector (1 bar, 60–90 s; PDES; NPI Electronic). Mice were anesthetized with a combination of isoflurane (0.5% vol/vol in 5% O_2) and ketamine (50 mg/ml; 10 µl bolus followed by 1.5 µl/min, administered i.p. through a catheter connected to a pump) and imaged using a Trim ScopeII microscope (LaVision) with three nondescanned detectors with bandpass filters (620/60, 460/80, and 525/50 nm) or an LSM 7MP (Zeiss) equipped with a Ti:Sa laser (Chameleon Ultra II; Coherent) with three bandpass filters (420/80, 500/550, and 565–610 nm) and one long-pass filter (555 nm). Fluorophores were excited at 800 nm. A 20× W Plan-Apochromat (NA 1.0; Zeiss) was used for both microscopes. Z stacks of the imaging region were taken (Trim ScopeII: XY, 250 × 250 µm, 828 px; Z, 1-µm step size, 100-µm range, pixel dwell time 0.93 µs; LSM 7MP: XY, 249.8 × 249.8 µm, 828 px; Z, 1-µm step size, 100-µm range, pixel dwell time 0.79 µs), followed by XY time-lapse series of calcium activity (Trim ScopeII: 260 × 260 µm, 250 px, pixel dwell time 1.9 µs, frequency 3.55 Hz; LSM 7MP: 249 × 249 µm, 240 px, pixel dwell time 2.14 µs, frequency 3.47 Hz) for 10 min at 800 nm. Laser power below the objective was kept between 20 and 40 mW to minimize laser-induced artifacts and phototoxicity.

Behavioral phenotyping

All data were recorded and analyzed with EthoVision XT9 (Noldus). For Barnes maze experiments, mice were placed in the center of a brightly lit open platform (diameter, 122 cm) in the presence of a continuous clicking sound. The platform was confined by 20 holes (hole diameter, 5 cm), with an escape box (target) fixed below one hole; all other holes were sealed. Extramaze cues were present for spatial orientation. 24 h before the first training day, the mice were placed in the middle of the platform and gently guided with a transparent glass beaker to the target. The beaker was placed on top of the target hole, and the mice were allowed 5 min to enter the escape box. Once the mice had entered the escape box, the clicking sound was stopped and they stayed in the escape box for 1 min. During the 4-d training/acquisition phase, mice performed four trials per day, with an intertrial interval of 15 min. For each trial, mice were put at the center of the platform in a black tube for 30 s in the presence of the clicking sound, and after tube removal were allowed to freely explore the maze until they entered the escape box, after which the sound was stopped. The mice had 180 s to find the escape box. Mice that were not able to find the box were guided to the escape box using the glass beaker and left in the box for 1 min. On day 5 (probe trial), the escape box was removed, the target hole was sealed, and the mice were allowed to freely explore the maze for 60 s.

Morris water maze experiments were conducted using a circular pool (diameter, 110 cm) filled with opacified water at 20°C. The maze was virtually divided into four quadrants, with one containing a hidden platform (diameter, 10 cm) 1 cm below the water surface. Extramaze cues were present for spatial orientation. Mice were

Downloaded from http://rupress.org/jem/article-pdf/215/6/1649/1760532/jem_20171487.pdf by guest on 08 February 2026

placed into the water in a quasi-random fashion and were allowed to search for the platform for 60 s and remain on the platform for 15 s; if the mice did not reach the platform in the allotted time, they were placed onto it manually. Mice were tested in four trials per day for five consecutive days with an intertrial interval of 30 min. Mice were dried with tissue towels and placed back in their home cages after the trials. For the probe trials, which were conducted 24 h after the last training session, the platform was removed, and mice were put in a new position into the maze and allowed to swim for 60 s.

Electrophysiology

Electrophysiological recordings were performed in acute brain slices as previously described (Minge et al., 2017). Briefly, 300-µm acute hippocampal slices were obtained from APPPS1 and age-matched WT littermates. Horizontal slices were cut in an ice-cold slicing solution containing (in mM) NaCl 60, sucrose 105, KCl 2.5, $MgCl_2$ 7, NaH_2PO_4 1.25, ascorbic acid 1.3, sodium pyruvate 3, $NaHCO_3$ 26, $CaCl_2$ 0.5, and glucose 10 (osmolarity 300–310 mOsm) and kept in the solution at 34°C for 15 min before being stored at room temperature (21–23°C) in an extracellular solution containing (in mM) NaCl 131, KCl 2.5, $MgSO_4$ 1.3, NaH_2PO_4 1.25, $NaHCO_3$ 21, $CaCl_2$ 2, and glucose 10. All solutions were constantly bubbled with 95% O_2/5% CO_2. Slices were allowed to rest for at least 1 h before recordings commenced, transferred to an interface chamber, and superfused with extracellular solution at 34°C. In a subset of experiments, MRS2197 (30 µM; Tocris) was added to the extracellular solution for 20–30 min before recordings started.

Field excitatory postsynaptic potentials (fEPSPs) were recorded through a standard patch pipette (3–4 MΩ) filled with extracellular solution and placed in the CA1 stratum radiatum. fEPSPs were evoked by electrical stimulation of CA3-CA1 Schaffer collaterals using a bipolar concentric stimulation electrode (FHC) placed in the stratum radiatum at the border between CA2/3 and CA1. The stimulation intensity was adjusted to obtain fEPSPs with half-maximum amplitude (without MRS2197: WT, 66.1 ± 4 µA, n = 12; APPPS1, 69.9 ± 7.6 µA, n = 8; Student's t test, P = 0.68; with MRS2197: WT, 39.7 ± 10.3 µA, n = 7; APPPS1, 46 ± 5.8 µA, n = 11; Student's t test, P = 0.52).

Basal synaptic transmission was monitored using single stimuli (100-µs duration) every 15 s for at least 10 min before induction of LTP using theta-burst stimulations (TBSs). During a TBS, eight bursts consisting of four stimuli (100 Hz) were applied at 5 Hz. TBS were delivered three times with an interval of 1 min. Subsequently, single stimuli were applied for 30 min to probe fEPSP potentiation.

Signals were amplified (1000×, EXT-02B; NPI) and filtered (high-pass, 0.1 Hz; low-pass, 20 kHz). Data were digitalized at a sampling rate of 10 kHz and stored using WinWCP (Strathclyde Electrophysiology Software). Analysis of fEPSP slopes was performed offline using Clampfit (Molecular Devices).

Immunohistochemistry

Mice were sacrificed, and one hemisphere was fixed in 4% paraformaldehyde for 1 d, stored in sucrose (15 and 25%), and embedded in Tissue-Tek (Sakura). Saggital sections (30 µm) were obtained using a cryostat (Thermo Fisher) and mounted onto slides.

Postmortem human brain tissue sections (4 µm) from AD cases were obtained through a collaboration with the Department of Neuropathology (University Hospital Bonn, Germany). The sections were deparaffined using xylene and descending ethanol solutions and incubated for 30 min in 0.21% citric acid (90–95°C).

All brain sections were blocked with 10% normal goat serum (Vector Labs) and 0.3% Triton X-100 (Sigma) in PBS for 1 h. Subsequently, mouse brain sections were incubated with rabbit anti-GFAP (1:500; Z0334; Dako), rabbit anti-P2Y1R (1:200; APR009; Almone), rat anti-GFAP (1:1,000; 130300; Invitrogen), mouse anti-IC16 (1:250; provided by C. Pietrzik, Mainz University, Mainz, Germany); rabbit anti-Iba1 (1:250; 019-19741; Wako), rabbit anti-synaptophysin (1:250; ab14692; Abcam), chicken anti-Homer1 (1:500; 160006; Synaptic Systems), and rat anti-LAMP1 (1:750; 121602; BioLegend) in 5% normal goat serum and 0.05% Triton X-100 overnight at 4°C. Human brain sections were incubated with rabbit anti-P2Y1R (1:100; APR009; Almone), rat anti-GFAP (1:250; 130300; Invitrogen), and mouse anti-IC16 (1:250). Nuclei were stained with Hoechst 33258 (1:1,000; Thermo Fisher). After rinsing human sections in Tris buffer and mouse sections in PBS, stainings were incubated with secondary antibodies from goat (anti–rabbit Alexa Fluor 594, anti–rat Alexa Fluor 633, anti–rabbit Alexa Fluor 488, anti–mouse Alexa Fluor 647, anti–rat Alexa Fluor 647, and anti–chicken Alexa Fluor 647; 1:1,000; Thermo Fisher) in PBS and 0.05% Triton X-100 for 1 h at room temperature, rinsed, and mounted in Fluoromount-G (Southern Biotech).

For thioflavin staining, sections were shortly incubated with 70 and 80% ethanol and stained with 1% thioflavin S (Sigma) in 80% ethanol for 15 min. Subsequently, sections were rinsed in 80 and 70% ethanol and distilled water, counterstained with Hoechst, and mounted as described above.

Images were acquired using either a confocal laser-scanning microscope (LSM 700; Zeiss) with a 40× (NA 1.3) or 63× (NA 1.4) objective or a slide scanner (Axio Scan.Z1, Zeiss) with a 10× objective (NA 0.45), with the following filter settings: LSM700, 490–555 BP, 640 LP, 490 SP; AxioScan.Z1, 470/40 BP, 525–50 BP, 587/25 BP, 647/70 BP, 640/30 BP, 690/50 BP. The same image acquisition settings were used for each staining.

Protein biochemistry

Mice were sacrificed, and one hemisphere was quickly transferred to liquid nitrogen and stored at −80°C. Protein extraction was performed by homogenization in PBS, pH 7.4, and 1% phosphatase inhibitor cocktail (Thermo Fisher) and 1% protease inhibitor cocktail (Thermo Fisher) using a ceramic bead homogenizer (Precellys; VWR). Homogenates were extracted in RIPA buffer (in mM: 49.96 Tris, pH 7.2, 149.6 NaCl, 25.6 NP-40, 24 Na deoxycholate, and 6.8 SDS) and centrifuged for 30 min at 100,000 *g*. The pellet containing insoluble Aβ was solubilized in SDS buffer (in mM: 69.2 SDS and 24.98 Tris, pH 7.5). Protein concentration was measured using a BCA Protein Assay kit (Thermo Fisher) and a FLUOstar Omega reader (BMG).

For protein gel electrophoresis, samples were solubilized in 4× LDS buffer (Life Technologies), boiled for 10 min at 95°C, centrifuged for 5 min at 20,000 *g* at 4°C, and loaded on 4–12% NuPAGE Novex Bis-Tris-midi gels (Life Technologies). SeeBlue Plus2–prestained protein standard (Thermo Fisher) was used to determine molecular weights. After electrophoresis, the samples were transferred to nitrocellulose membranes (0.2 µm; Bio-Rad). For CTF detection, the membranes were incubated for 1 min in 1× Tris-buffered saline

Downloaded from http://rupress.org/jem/article-pdf/215/6/1649/1760532/jem_20171487.pdf by guest on 08 February 2026

(2.73 M NaCl and 39.9 mM Tris, 96°C, pH 7.6). All membranes were blocked in 5% nonfat skim milk powder (Biomol) in 1× Tris-buffered saline with 0.05% Tween 20 (Merck) for 1 h at room temperature. Full-length APP was detected using 6E10 antibody (1:100,000; SIG-39320-1000; BioLegend), CTFs were detected using C1/6.1 antibody (1:1,000; 802801, BioLegend), neprilysin was detected using an anti-CD10 antibody (1:500; AF1126, R&D Systems), and actin was detected using an anti–β-actin antibody (1:8,000; A2103; Sigma). Immunoreactivity was detected by enhanced chemiluminescence reaction (Stella 3200; Raytest).

ELISA quantification of P2Y1R was conducted using whole-brain homogenates (25 mg/ml) according to the manufacturer's instructions (EL017326MO; Cusabio). Quantitative determination of Aβ was performed using an electrochemiluminescence triplex ELISA for $Aβ_{1–38}$, $Aβ_{1–40}$, and $Aβ_{1–42}$ (Aβ Peptide Panel 1 6E10 Kit; Meso Scale Discovery) according to the manufacturer's instructions using a SECTOR Imager 2400 reader (Meso Scale Discovery).

Data analysis

Data analysis was conducted blinded for pharmacological intervention or genotype. Calcium imaging data were imported into ImageJ 1.50i (National Institutes of Health) and stabilized using the Image Stabilizer plugin for ImageJ (K. Li, Carnegie Mellon University, Pittsburgh, PA). Regions of interest (ROIs) of OGB-1–positive cells and GCaMP6f-expressing astrocytes were defined manually. OGB-1–positive cells were considered astrocytes when they were colabeled with SR101. Neurons were identified manually by their morphology and the absence of SR101. For all calcium data, fluorescence over time was determined for each ROI, converted to $\Delta F/F$, and imported into Matlab R2013b (MathWorks). After removal of outliers using a median filter and smoothing using a Gaussian filter, peak amplitude, time to peak, peak to baseline, and full duration at half maximum (FDHM) were determined for each signal using a custom-written algorithm in Matlab. Each time-lapse series that met this criterion was plotted together with the respective video file for visual inspection and verification. Astrocytes were defined as hyperactive based on established criteria (activity, ≥0.4 events/min; Delekate et al., 2014).

All immunohistochemical data points represent mean values of 5–10 brain sections per mouse. Immunohistochemical images were imported into ImageJ, converted to 8-bit gray level images, and smoothed using a Gaussian filter. After contrast enhancement (0.4% saturated pixels), images were binarized using ImageJ (plaque stainings, automated MaxEntropy algorithm; synaptic puncta stainings, automated Otsu algorithm; for GFAP and Iba1, a threshold defined as the mean background intensity plus the SD of background intensity multiplied by 2 was used). Astrocyte, microglia, and plaque area coverage as well as the number and size of plaques and LAMP1-positive dystrophic dendrites per area were quantified using ImageJ. The plaque area was subtracted from the area covered by dystrophic neurites before data analysis. To quantify synaptic puncta, colocalized synaptophysin-positive or Homer1-positive punctuate signals were counted in thresholded single-plane confocal images using the Synapse Counter plugin for ImageJ (Dzyubenko et al., 2016) with a predefined puncta size range of 0.9–20 μm^2. For periplaque morphological complexity quantification, high-resolution stacks were subjected to background removal (plaque stainings, automated Otsu algorithm; GFAP/Iba1 stainings, automated Huang algorithm; intensity thresholds were calculated based on maximum-intensity projections), and for each channel, 3D particles (plaque channel, ≥600 voxels; glia channel, ≥30 voxels) were reconstructed using a Flood-Filler algorithm. Plaque mean intensity was calculated by the mean of all plaque voxels. Glial particles were considered as periplaque when they contained ≥1 voxels with a distance ≤2r to the plaque center. Near-plaque glial particles were smoothed using a Gaussian filter (sigma, 1.0 px), skeletonized using the Skeletonize3D plugin, and analyzed using the Analyze Skeleton plugin.

We used Mann–Whitney test or Student's t test for comparisons between two groups; Kruskal–Wallis test followed by Dunn's multiple comparisons test or one-way ANOVA and Dunnett's multiple comparison test to compare several groups; two-way repeated-measures ANOVA and Bonferroni post hoc test for multiple measurements in the same groups; Fisher's exact test to compare proportions; Kolmogorov–Smirnov test to compare cumulative distributions; and Spearman correlation coefficient to quantify correlations. Data were analyzed using Prism 7 (GraphPad) and are expressed as mean ± SEM. $P < 0.05$ was accepted as statistically significant.

Online supplemental material

Fig. S1 shows that the anti-P2Y1R antibody displayed immunoreactivity for astrocytes in WT mice, but not in *P2y1r*$^{-/-}$ mice. Fig. S2 shows the workflow for the quantification of morphological barrier functions of periplaque astrocytes. Video 1 shows spontaneously active astrocytes in the hippocampus of an APPPS1 mouse.

Acknowledgments

We thank Sybille Krauss, Christoph Moehl, and Michael Heneka (German Center for Neurodegenerative Diseases [DZNE], Bonn, Germany) for technical help; Mathias Jucker for providing the APPPS1 mouse line; Schuichi Koizumi and Ute Krügel for providing *P2y1r*$^{-/-}$ mice; Ju Chen for providing *Ip3r2*$^{-/-}$ mice; and Claus Pietrzik for providing the IC16 antibody.

This work was supported by grants to G.C. Petzold from the European Union (EU) Joint Program, Neurodegenerative Disease Research program (JPND; Horizon 2020 Framework Programme, grant agreement 643417/DACAPO-AD), the Alzheimer Forschung Initiative (AFI), and the DZNE. A. Halle is member of the German Research Foundation (DFG)–funded Cluster of Excellence ImmunoSensation (EXC 1023). C. Henneberger was supported by the North Rhine-Westphalia Rückkehrerprogramm. C. Henneberger and M. Fuhrmann were supported by DFG (SFB1089).

The authors declare no competing financial interests.

Author contributions: G.C. Petzold conceptualized and supervised the study with technical input from M. Fuhrmann, C. Henneberger, K. Keppler, and A. Halle; N. Reichenbach and G.C. Petzold established the methodology, analyzed data, and wrote the manuscript with input from all other authors. N. Reichenbach, A. Delekate, B. Breithausen, S. Poll, T. Schulte, J. Peter, M. Plescher, J.N. Hansen, and N. Blank carried out the experiments and analyzed data.

Downloaded from http://rupress.org/jem/article-pdf/215/6/1649/1760532/jem_20171487.pdf by guest on 08 February 2026

Submitted: 14 August 2017
Revised: 12 February 2018
Accepted: 12 April 2018

References

Araque, A., G. Carmignoto, P.G. Haydon, S.H. Oliet, R. Robitaille, and A. Volterra. 2014. Gliotransmitters travel in time and space. *Neuron.* 81:728–739. https://doi.org/10.1016/j.neuron.2014.02.007

Boyer, J.L., A. Mohanram, E. Camaioni, K.A. Jacobson, and T.K. Harden. 1998. Competitive and selective antagonism of P2Y1 receptors by N6-methyl 2′-deoxyadenosine 3′,5′-bisphosphate. *Br. J. Pharmacol.* 124:1–3. https://doi.org/10.1038/sj.bjp.0701837

Busche, M.A., G. Eichhoff, H. Adelsberger, D. Abramowski, K.-H. Wiederhold, C. Haass, M. Staufenbiel, A. Konnerth, and O. Garaschuk. 2008. Clusters of hyperactive neurons near amyloid plaques in a mouse model of Alzheimer's disease. *Science.* 321:1686–1689. https://doi.org/10.1126/science.1162844

Chhatriwala, M., R.G. Ravi, R.I. Patel, J.L. Boyer, K.A. Jacobson, and T.K. Harden. 2004. Induction of novel agonist selectivity for the ADP-activated P2Y1 receptor versus the ADP-activated P2Y12 and P2Y13 receptors by conformational constraint of an ADP analog. *J. Pharmacol. Exp. Ther.* 311:1038–1043. https://doi.org/10.1124/jpet.104.068650

Condello, C., A. Schain, and J. Grutzendler. 2011. Multicolor time-stamp reveals the dynamics and toxicity of amyloid deposition. *Sci. Rep.* 1:19. https://doi.org/10.1038/srep00019

Condello, C., P. Yuan, A. Schain, and J. Grutzendler. 2015. Microglia constitute a barrier that prevents neurotoxic protofibrillar Aβ42 hotspots around plaques. *Nat. Commun.* 6:6176. https://doi.org/10.1038/ncomms7176

Delekate, A., M. Füchtemeier, T. Schumacher, C. Ulbrich, M. Foddis, and G.C. Petzold. 2014. Metabotropic P2Y1 receptor signalling mediates astrocytic hyperactivity in vivo in an Alzheimer's disease mouse model. *Nat. Commun.* 5:5422. https://doi.org/10.1038/ncomms6422

Domercq, M., L. Brambilla, E. Pilati, J. Marchaland, A. Volterra, and P. Bezzi. 2006. P2Y1 receptor-evoked glutamate exocytosis from astrocytes: Control by tumor necrosis factor-alpha and prostaglandins. *J. Biol. Chem.* 281:30684–30696. https://doi.org/10.1074/jbc.M606429200

Dzyubenko, E., A. Rozenberg, D.M. Hermann, and A. Faissner. 2016. Colocalization of synapse marker proteins evaluated by STED-microscopy reveals patterns of neuronal synapse distribution in vitro. *J. Neurosci. Methods.* 273:149–159. https://doi.org/10.1016/j.jneumeth.2016.09.001

Franke, H., A. Verkhratsky, G. Burnstock, and P. Illes. 2012. Pathophysiology of astroglial purinergic signalling. *Purinergic Signal.* 8:629–657. https://doi.org/10.1007/s11302-012-9300-0

Gengler, S., A. Hamilton, and C. Hölscher. 2010. Synaptic plasticity in the hippocampus of a APP/PS1 mouse model of Alzheimer's disease is impaired in old but not young mice. *PLoS One.* 5:e9764. https://doi.org/10.1371/journal.pone.0009764

Heneka, M.T., M.J. Carson, J. El Khoury, G.E. Landreth, F. Brosseron, D.L. Feinstein, A.H. Jacobs, T. Wyss-Coray, J. Vitorica, R.M. Ransohoff, et al. 2015. Neuroinflammation in Alzheimer's disease. *Lancet Neurol.* 14:388–405. https://doi.org/10.1016/S1474-4422(15)70016-5

Jourdain, P., L.H. Bergersen, K. Bhaukaurally, P. Bezzi, M. Santello, M. Domercq, C. Matute, F. Tonello, V. Gundersen, and A. Volterra. 2007. Glutamate exocytosis from astrocytes controls synaptic strength. *Nat. Neurosci.* 10:331–339. https://doi.org/10.1038/nn1849

Kuchibhotla, K.V., S.T. Goldman, C.R. Lattarulo, H.-Y. Wu, B.T. Hyman, and B.J. Bacskai. 2008. Abeta plaques lead to aberrant regulation of calcium homeostasis in vivo resulting in structural and functional disruption of neuronal networks. *Neuron.* 59:214–225. https://doi.org/10.1016/j.neuron.2008.06.008

Kuchibhotla, K.V., C.R. Lattarulo, B.T. Hyman, and B.J. Bacskai. 2009. Synchronous hyperactivity and intercellular calcium waves in astrocytes in Alzheimer mice. *Science.* 323:1211–1215. https://doi.org/10.1126/science.1169096

Li, X., A.V. Zima, F. Sheikh, L.A. Blatter, and J. Chen. 2005. Endothelin-1-induced arrhythmogenic Ca2+ signaling is abolished in atrial myocytes of inositol-1,4,5-trisphosphate (IP3)-receptor type 2-deficient mice. *Circ. Res.* 96:1274–1281. https://doi.org/10.1161/01.RES.0000172556.05576.4c

Liddelow, S.A., K.A. Guttenplan, L.E. Clarke, F.C. Bennett, C.J. Bohlen, L. Schirmer, M.L. Bennett, A.E. Münch, W.S. Chung, T.C. Peterson, et al. 2017. Neurotoxic reactive astrocytes are induced by activated microglia. *Nature.* 541:481–487. https://doi.org/10.1038/nature21029

Minge, D., O. Senkov, R. Kaushik, M.K. Herde, O. Tikhobrazova, A.B. Wulff, A. Mironov, T.H. van Kuppevelt, A. Oosterhof, G. Kochlamazashvili, et al. 2017. Heparan sulfates support pyramidal cell excitability, synaptic plasticity, and context discrimination. *Cereb. Cortex.* 27:903–918. https://doi.org/10.1093/cercor/bhx003

Ortinski, P.I., J. Dong, A. Mungenast, C. Yue, H. Takano, D.J. Watson, P.G. Haydon, and D.A. Coulter. 2010. Selective induction of astrocytic gliosis generates deficits in neuronal inhibition. *Nat. Neurosci.* 13:584–591. https://doi.org/10.1038/nn.2535

Palop, J.J., and L. Mucke. 2016. Network abnormalities and interneuron dysfunction in Alzheimer disease. *Nat. Rev. Neurosci.* 17:777–792. https://doi.org/10.1038/nrn.2016.141

Palop, J.J., J. Chin, E.D. Roberson, J. Wang, M.T. Thwin, N. Bien-Ly, J. Yoo, K.O. Ho, G.-Q. Yu, A. Kreitzer, et al. 2007. Aberrant excitatory neuronal activity and compensatory remodeling of inhibitory hippocampal circuits in mouse models of Alzheimer's disease. *Neuron.* 55:697–711. https://doi.org/10.1016/j.neuron.2007.07.025

Petzold, G.C., and V.N. Murthy. 2011. Role of astrocytes in neurovascular coupling. *Neuron.* 71:782–797. https://doi.org/10.1016/j.neuron.2011.08.009

Pompl, P.N., M.J. Mullan, K. Bjugstad, and G.W. Arendash. 1999. Adaptation of the circular platform spatial memory task for mice: Use in detecting cognitive impairment in the APP(SW) transgenic mouse model for Alzheimer's disease. *J. Neurosci. Methods.* 87:87–95. https://doi.org/10.1016/S0165-0270(98)00169-1

Radde, R., T. Bolmont, S.A. Kaeser, J. Coomaraswamy, D. Lindau, L. Stoltze, M.E. Calhoun, F. Jäggi, H. Wolburg, S. Gengler, et al. 2006. Abeta42-driven cerebral amyloidosis in transgenic mice reveals early and robust pathology. *EMBO Rep.* 7:940–946. https://doi.org/10.1038/sj.embor.7400784

Reiman, E.M., Y.T. Quiroz, A.S. Fleisher, K. Chen, C. Velez-Pardo, M. Jimenez-Del-Rio, A.M. Fagan, A.R. Shah, S. Alvarez, A. Arbelaez, et al. 2012. Brain imaging and fluid biomarker analysis in young adults at genetic risk for autosomal dominant Alzheimer's disease in the presenilin 1 E280A kindred: A case-control study. *Lancet Neurol.* 11:1048–1056. https://doi.org/10.1016/S1474-4422(12)70228-4

Robel, S., and H. Sontheimer. 2016. Glia as drivers of abnormal neuronal activity. *Nat. Neurosci.* 19:28–33. https://doi.org/10.1038/nn.4184

Sanchez, P.E., L. Zhu, L. Verret, K.A. Vossel, A.G. Orr, J.R. Cirrito, N. Devidze, K. Ho, G.-Q. Yu, J.J. Palop, and L. Mucke. 2012. Levetiracetam suppresses neuronal network dysfunction and reverses synaptic and cognitive deficits in an Alzheimer's disease model. *Proc. Natl. Acad. Sci. USA.* 109:E2895–E2903. https://doi.org/10.1073/pnas.1121081109

Schmid, L.C., M. Mittag, S. Poll, J. Steffen, J. Wagner, H.-R. Geis, I. Schwarz, B. Schmidt, M.K. Schwarz, S. Remy, and M. Fuhrmann. 2016. Dysfunction of somatostatin-positive interneurons associated with memory deficits in an Alzheimer's disease model. *Neuron.* 92:114–125. https://doi.org/10.1016/j.neuron.2016.08.034

Sharp, A.H., F.C. Nucifora Jr., O. Blondel, C.A. Sheppard, C. Zhang, S.H. Snyder, J.T. Russell, D.K. Ryugo, and C.A. Ross. 1999. Differential cellular expression of isoforms of inositol 1,4,5-triphosphate receptors in neurons and glia in brain. *J. Comp. Neurol.* 406:207–220. https://doi.org/10.1002/(SICI)1096-9861(19990405)406:2%3C207::AID-CNE6%3E3.0.CO;2-7

Shi, Q., S. Chowdhury, R. Ma, K.X. Le, S. Hong, B.J. Caldarone, B. Stevens, and C.A. Lemere. 2017. Complement C3 deficiency protects against neurodegeneration in aged plaque-rich APP/PS1 mice. *Sci. Transl. Med.* 9:eaaf6295. https://doi.org/10.1126/scitranslmed.aaf6295

Sperling, R.A., P.S. Laviolette, K. O'Keefe, J. O'Brien, D.M. Rentz, M. Pihlajamaki, G. Marshall, B.T. Hyman, D.J. Selkoe, T. Hedden, et al. 2009. Amyloid deposition is associated with impaired default network function in older persons without dementia. *Neuron.* 63:178–188. https://doi.org/10.1016/j.neuron.2009.07.003

Thrane, A.S., V. Rangroo Thrane, D. Zeppenfeld, N. Lou, Q. Xu, E.A. Nagelhus, and M. Nedergaard. 2012. General anesthesia selectively disrupts astrocyte calcium signaling in the awake mouse cortex. *Proc. Natl. Acad. Sci. USA.* 109:18974–18979. https://doi.org/10.1073/pnas.1209448109

Vossel, K.A., K.G. Ranasinghe, A.J. Beagle, D. Mizuiri, S.M. Honma, A.F. Dowling, S.M. Darwish, V. Van Berlo, D.E. Barnes, M. Mantle, et al. 2016. Incidence and impact of subclinical epileptiform activity in Alzheimer's disease. *Ann. Neurol.* 80:858–870. https://doi.org/10.1002/ana.24794

Yuan, P., C. Condello, C.D. Keene, Y. Wang, T.D. Bird, S.M. Paul, W. Luo, M. Colonna, D. Baddeley, and J. Grutzendler. 2016. TREM2 haplodeficiency in mice and humans impairs the microglia barrier function leading to decreased amyloid compaction and severe axonal dystrophy. *Neuron.* 90:724–739. https://doi.org/10.1016/j.neuron.2016.05.003

Zhang, D., Z.-G. Gao, K. Zhang, E. Kiselev, S. Crane, J. Wang, S. Paoletta, C. Yi, L. Ma, W. Zhang, et al. 2015. Two disparate ligand-binding sites in the human P2Y1 receptor. *Nature.* 520:317–321. https://doi.org/10.1038/nature14287

Downloaded from http://rupress.org/jem/article-pdf/215/6/1649/1760532/jem_20171487.pdf by guest on 08 February 2026